Supplementary Information

Accelerating Water Oxidation – A Mixed Co/Fe Polyoxometalate with Improved Turnover Characteristics

Joaquín Soriano-López,*[a,†] Friedrich W. Steuber,[a] Muhamed Mulahmetović,[a] Maria Besora,[b] Juan Modesto Clemente-Juan,[c] Mariah O' Doherty,[a] Nian-Yong Zhu,[a] Craig L. Hill,[d] Eugenio Coronado,[c] Josep M. Poblet,[b] and Wolfgang Schmitt,*[a]

[a] School of Chemistry & SFI AMBER Centre, Trinity College, University of Dublin, Ireland.

[b] Departament de Química Física i Inorgànica, Universitat Rovira i Virgili, Marcel·lí Domingo 1, 43007 Tarragona, Spain.

[c] Institut de Ciència Molecular, Universitat de València, Catedrático José Beltrán 2, 46980 Paterna, Spain

[d] Department of Chemistry, Emory University, 1515 Dickey Dr., Atlanta, Georgia, 30322, United States.

†Current address: Institut de Ciència Molecular, Universitat de València, Catedrático José Beltrán 2, Paterna 46980, Spain.

*Correspondence to: joaquin.soriano@uv.es, schmittw@tcd.ie

Table of Contents

1) Instrumentation and Methodology

Single crystal X-ray diffraction: Crystals of suitable size for single crystal X-ray diffraction measurements were mounted on a MiTiGen micromount. Intensity data was collected on a Bruker APEX DUO equipped with an APEX II CCD detector and a sealed tube Mo-Kα (λ = 0.71073 Å) X-ray source with a graphite monochromator. Temperature control was accomplished with an Oxford Cryostream Cobra LT unit. Intensity data was processed with SAINT+[1] and corrected for absorption by multi-scan methods using SADABS.[2] Structure solution was accomplished using intrinsic phasing as implemented in SHELXT[3] and refinement on F^2 with full-matrix least squares procedures was carried out with SHELXL-2013[4] in Olex2.[5]

Fourier-Transform Infrared (FT-IR) spectroscopy: FT-IR spectra were recorded using a Bruker Tensor II FT-IR spectrometer with a scan rate of 16 scans min^{-1} in a spectral range of 400-4000 cm^{-1}.

Raman spectroscopy: Raman spectroscopy measurements were performed using a Renishaw-1000 micro-Raman spectrometer equipped with a magnification objective (50×) and a cooled CCD camera system, which was calibrated prior to measurements using an internal Si standard. The spectral resolution of the spectrometer was 1 cm^{-1}. Each spectrum was averaged over 5 measurements with an accumulation time of 10 seconds and analysed using the Renishaw WIRE software package. All samples were excited using a 785 nm laser.

Thermogravimetric analysis (TGA): TGA was performed using Perkin Elmer Pyris-1 Thermogravimetric analyser under a continuous flow of N_2. The sample was held at 30 ˚C for 1 minute, followed by heating up to 500 ˚C at 3 ˚C /minute.

Powder X-ray diffraction (PXRD): PXRD data was collected at room temperature using a Bruker D2 Phaser diffractometer equipped with a CuKα X-ray source.

X-ray photoelectron spectroscopy (XPS): XPS measurements were performed at SSTTI University of Alicante (Spain). The sample surfaces were analysed with an XPS, K-ALPHA, Thermo Scientific. All spectra were collected using Al-Kα radiation (1486.6 eV), monochromatised by a twin crystal monochromator, which yields a focused X-ray spot with 400 µm of diameter, at 3 mA × 12 kV. The alpha hemispherical analyser was operated in the constant energy mode with survey scan pass energies of 200 eV to measure the whole energy band and 50 eV in a narrow scan to selectively measure individual elements. Charge compensation was achieved with the system flood gun that provides low energy electrons and low energy argon ions from a single source.

Energy-dispersive X-ray spectroscopy (EDX): EDX elemental analysis was carried out in a Zeiss ULTRA plus Scanning Electron Microscope equipped with a 20mm^2 Oxford Inca EDX detector.

Magnetic measurements: Variable-temperature susceptibility measurements were carried out in the temperature range 2–300 K on a magnetometer equipped with a SQUID sensor (Quantum Design MPMS-XL-5) under a magnetic field of 0.1 T.

Inductively coupled plasma – mass spectrometry (ICP-MS): Elemental analysis was conducted using an Agilent 7700x inductively coupled plasma mass spectrometer at University of Alicante.

2) Strucutre-Reactivity relationships of Co-based POMs and analogous structures

The following table has been assembled for comparative purposes considering selected Co-based POMs containing either monolacunary α-Keggin or trilacunary B-α-Keggin moieties, and their analogous derivatives of which the OER activity has been reported. The structures of those POMs with varying nuclearity are depicted below:

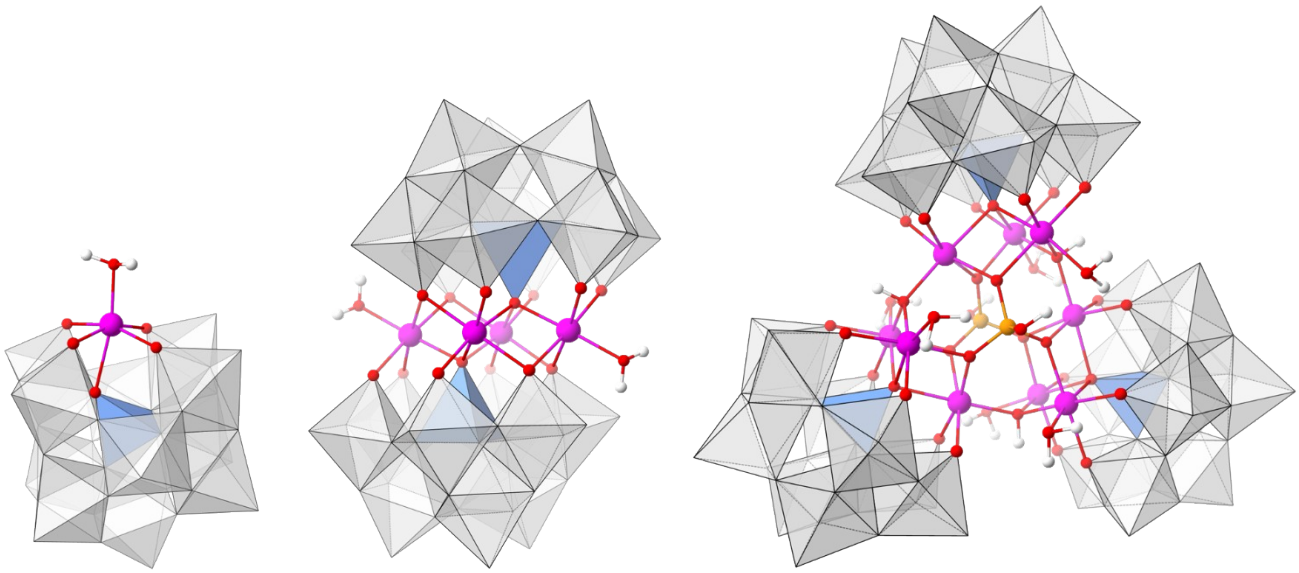

$[M(H_2O)XW_{11}O_{39}]^{n-}$ $[M_4(H_2O)_2(XW_9O_{34})_2]^{n-}$ $[M_9(H_2O)_6(OH)_3(HPO_4)_2(XW_9O_{34})_3]^{n-}$

Where M refers to the transition metal-substituted atoms and X are the heteroatoms. Colour code: M = pink; X = blue; W (addenda atoms) = grey; P = orange; O = red; H = white.

- The structure of $[M(H_2O)XW_{11}O_{39}]^{n-}$ consists of a monolacunary α-Keggin unit encapsulating a metal ion that is directly bound to a water molecule.

- $[M_4(H_2O)_2(XW_9O_{34})_2]^{n-}$ corresponds to the Weakley-sandwich structure, in which two trilacunary B-α-Keggin archetypes are stabilising a rhombic tetranuclear oxo-bridged *butterfly* moiety with two water molecules, each binding to the external metal atoms.

- $[M_9(H_2O)_6(OH)_3(HPO_4)_2(XW_9O_{34})_3]^{n-}$ is composed of three trilacunary B-α-Keggin moieties where the nonanuclear metal oxo core forms a triangle of triangles held together by two phosphate and three hydroxyl ligands. Six water molecules which bind to six different metal atoms complete the structure.

Nuclearity (# Keggin units)	Polyoxometalate	Variable	OER Conditions	Comments	Refs.
1		**Heteroatom**			
	$[Co(H_2O)XW_{11}O_{39}]^{n-}$	Co^{II}	Light-Induced OER: LED lamp (λ ≥ 420 nm), 16 mW; 15 μM POM, 1.0 mM $[Ru(bpy)_3]^{2+}$, 5.0 mM	• Only Co^{III} shows activity • P^V is active in the solid-state • Co^{II} is unstable	6
		Co^{III}			
		Si^{IV}			
		P^V			
		Metal			
	$[M(H_2O)PW_{11}O_{39}]^{n-}$	Fe^{III}	Electrocatalytic OER: Modified carbon paste electrodes with the Ba^{2+} salts; 50 mM KP_i buffer pH 6.9, 1 M KNO_3	• Co^{II} requires 60 mV less than Fe^{III} to reach 1 mA/cm^2	7
		Co^{II}			
2		**Heteroatom**			
	$[Co_4(H_2O)_2(XW_9O_{34})_2]^{n-}$	Si^{IV}	Light-Induced OER: LED lamp (λ = 470 nm); 20 μM POM, 1.0 mM $[Ru(bpy)_3]^{2+}$, 5.0 mM $Na_2S_2O_8$, 20 mM Na_2SiF_6 buffer (initial pH 5.8)	• Si^{IV} is much less efficient than P^V • The final O_2 yield using V^V is twice as high as that using P^V • V^V possesses a smaller ligand field within the tetra-cobalt core and a cobalt-to-vanadium charge transfer band, which decreases the activation energy on the O-O bond formation step	8
		P^V	Light-Induced OER: LED lamp (λ = 455 nm), 42.5 mW/cm^{-2}; 2 μM POM 1.0 mM $[Ru(bpy)_3]^{2+}$, 5.0 mM $Na_2S_2O_8$, 80 mM NaB_i (initial pH 9.0)		9–11
		V^V			
		Addenda			
	$[Co_4(H_2O)_2(PM''_9O_{34})_2]^{10-}$	W_{18}	Electrocatalytic OER: Nafion ink employing the Cs^+ salts drop cast on a glassy carbon electrode; 50 mM KP_i buffer pH 7.1,	• Increasing the amount of Mo in the addenda atoms increases the OER activity • Decrease of up to 188 mV at 1 mA/cm^2 with respect to W_{18}	12
		$W_{11}Mo_7$			
		$W_{10.4}Mo_{7.6}$			
		$W_{10}Mo_8$			
		Metal			
	$[M_4(H_2O)_2(PW_9O_{34})_2]^{n-}$	Mn^{II}	Electrocatalytic OER: 1 mM POM, 50 mM NaP_i buffer pH 7.0, 1 M $NaNO_3$	• Ni_4 is inactive • Initial activity of Mn_4 is comparable to that of Co_4, although it is unstable • Co_4 possesses an intrinsically higher electrocatalytic surface area than the Fe_4 derivative • Fe_4 requires 50 mV more than Co_4 mV at 1 mA/cm^2 • The activation energy for the O-O bond formation is lower for Co_4 than Fe_4, which results in a faster kinetics for the O_2 evolution	13
		Fe^{III}	Electrocatalytic OER: Modified carbon paste electrodes with the Ba^{2+} salts; 50 mM KP_i buffer pH 6.9, 1 M KNO_3		7
		Co^{II}			
		Ni^{II}	Light-Induced OER: LED lamp (λ = 455 nm), 42.5 mW/cm^{-2}; 10 μM POM 1.0 mM $[Ru(bpy)_3]^{2+}$, 5.0 mM $Na_2S_2O_8$, 80 mM NaB_i (initial pH 8.0)		14
		Mixed Metal			
	$[M_{4-x}M'_x(H_2O)_2(PW_9O_{34})_2]^{10-}$	Co_2Ni_2	Light-Induced OER: LED lamp (λ = 455 nm), 42.5 mW/cm^{-2}; 10 μM POM 1.0 mM $[Ru(bpy)_3]^{2+}$, 5.0 mM $Na_2S_2O_8$, 80 mM	• Co_2Ni_2 is an order of magnitude faster than Co_4 • Stronger orbital interaction between Ni and Co in Co_2Ni_2 acts to stabilise the peroxo	14

			NaB_i (initial pH 8.0)	formation free-energy reaction path, thus increasing its OER kinetics with respect to Co_4 • Co_2Mn_2 shows a lower OER activity than Co_4 (although not directly compared) • Ni_2Mn_2 possesses very low activity • Zn_2Mn_2 in inactive	
		Co_2Mn_2	Light-Induced OER: LED lamp (λ = 450 nm); 20 µM POM, 1.0 mM $[Ru(bpy)_3]^{2+}$, 5.0 mM $Na_2S_2O_8$, 80 mM NaB_i (initial pH 9.0)		15
		Ni_2Mn_2			
		Zn_2Mn_2			
3		**Heteroatom**			
	$[Co_9(H_2O)_6(OH)_3(HPO_4)_2(\mathbf{X}W_9O_{34})_3]^{n-}$	Ge^{IV}	Electrocatalytic OER: Modified carbon paste electrodes with the Cs^+ salts; 50 mM NaP_i buffer pH 7.0, 1 M NaO_3	• Ge^{IV} shows an intrinsic higher catalytic activity than P^V • Replacing P^V by Ge^{IV} increases the negative charge density of the POM, causing an increase in the energy levels of the molecular orbitals. This renders a more facile oxidation of the Co active centre	16
		P^V			

3) Electrochemical Procedures

Electrochemical measurements were performed using a Biologic VSP potentiostat. All the measurements were carried out in a 50 mM potassium phosphate (KP_i) buffer solution using KNO_3 (1 M) as electrolyte at pH 7.2. Ohmic drop (iR drop) compensations (85%) were applied prior to each experiment (except for differential pulse voltammetry (DPV) and rotating ring disk electrode (RRDE) measurements in bipotentiostat mode) using the positive feedback compensation method as implemented in the instrumental setup. A three-electrode set-up was used for all the experiments, except for the RRDE experiments (vide infra); Ag/AgCl (KCl 3M) was employed as the reference electrode, and a Pt wire counter electrode (a Pt mesh was used for bulk water electrolysis experiments). Either glassy carbon (GC) or carbon paste (CP) electrodes were employed as working electrodes, both with a surface area of 0.07 cm^2, as stated in the main text. Linear sweep voltammetry (LSV) and RRDE experiments were performed using an ALS RRDE-3A set-up connected to the Biologic VSP potentiostat with a 1 mV s^{-1} scan rate, and at 1,600 and 700 rpm, respectively. LSV data was used for Tafel analyses. RRDE experiments were carried out in the bipotentiostat mode with two working electrodes: GC (disk) and Pt (disk). Cyclic voltammograms (CVs), DPV, and RRDE measurements were performed under N_2 atmosphere, where the solutions were purged for at least 10 minutes prior to each measurement. The CVs were performed at a scan rate of 100 mV s^{-1}. Chronopotentiometric measurements were performed in an H-cell where the working and reference electrodes were separated from the counter electrode by a glass frit (P0).

The Nernst equation was used to calculate the thermodynamic water oxidation potential ($E^{0}_{H_2O/O_2}$) at the working pH:

$$E^{0}_{H_2O/O_2} = 1.229 - (0.059 \times pH)\ (V)\ vs\ NHE\ at\ 25\ ^{\circ}C \quad \text{(Eq. S1)}$$

All applied potentials (E_{app}) were converted to the NHE reference scale using $E_{NHE} = E_{Ag/AgCl} + 0.210\ (V)$. The overpotentials were calculated by subtracting the thermodynamic H_2O oxidation potential ($E^{0}_{H_2O/O_2}$) from E_{app} as:

$$\eta = E_{app} - E^{0}_{H_2O/O_2} \quad \text{(Eq. S2)}$$

All current densities were calculated based on the geometrical surface area of the electrodes. The onset potentials were estimated from the intersection point between the tangent lines of the Faradaic current at 0.2 mA cm^{-2} and the non-Faradic current. Herein all the potentials are given versus NHE, unless otherwise stated.

Preparation of the Nafion ink electrodes: 5 mg of catalyst were mixed with 5 mg of acetylene carbon black 50% compressed (Strem Chemicals UK Ltd.) and added into 900 µL of a 3:1 (H_2O:2-propanol) solution. 100 µL of a Nafion® 117 solution (~5%) were also added and the mixture was sonicated for 2 h to obtain a homogeneous suspension. Aliquots of the mixture were deposited on the electrode surface and dried at 70 °C for 5 minutes. Aliquots of 5 µL were used for glassy carbon electrodes with a surface area of 0.07 cm^2, whereas 10 µL were employed for RRDE with a glassy carbon disk electrode with a surface area of 0.196 cm^2.

Preparation of the Carbon Paste electrodes: The corresponding quantities of the catalysts were dispersed in carbon paste (ALS, Carbon Paste Oil) in an agate mortar to obtain a homogeneous carbon blend, which was subsequently introduced into the carbon paste electrode pocket (surface area of 0.07 cm^2). The surface of the electrode was polished with satin weighing paper to obtain a smooth surface. The electrodes were weighed before and after introducing the carbon blend into the pocket allowing the calculation of the catalyst quantity in respective blends.

Catalyst recovery and post-catalytic characterisation: In order to minimise the loss of any electrode-bound species that may have been formed during the reaction as best as possible, we did not separate the Ba-POM from the carbon paste. Therefore, after the long-term chronopotentiometric experiments, the electrodes were rinsed with water to avoid the crystallisation of any salt arising from the KP_i buffer, and the electrode was left to dry in ambient conditions. Afterwards, Raman spectroscopy was performed directly on the surface of the modified carbon paste electrode, whereby only the POM could be identified. Other species, e.g. POM-derived metal oxides, could not be detected at the electrode surface. Following, we recovered the outer part of the POM-carbon paste blend that was introduced into the pocket of the carbon paste electrode (*ca*. 25% of the total employed), since water does not penetrate through the whole electrode pocket. Hence, this recovered portion is considered as the truly reactive part of the electrode since it is in close contact with water, and any hypothetical POM transformation should occur in this space. This POM-carbon paste blend was left under vacuum overnight, whereby most of the paraffin oil was removed. The resulting powder was then subjected to further characterisation, *i.e.* by IR spectroscopy, XPS analysis and EDX spectroscopy.

Quantification of the oxygen evolved: An Ocean Optics NeoFOX oxygen sensing system equipped with a FOXY probe was used to quantify the evolving quantity of O_2. The FOXY probe was calibrated by a two-point calibration procedure using a 0% O_2 reference under a N_2 atmosphere and a 20.9% O_2 reference measured in the air. The experiments were carried out in a two-neck round bottom flask (total volume of 50 mL). The FOXY probe was inserted into the gas space ($V_{Gas\ space}$ ≈ 23 mL). A N_2 flow was used to completely deaerate the solution. After purging the solution for at least 1h, the N_2 flow was removed and a base line for 30 minutes was recorded before starting the chronopotentiometry at a constant current density of 1 mA/cm^2. The evolving O_2 quantity was measured for 4h, after which the experiment was stopped and the O_2 production ceased, as confirmed by the plateau observed at the end of the experiment. This observation indicates that the O_2 measured exclusively arises from the electrocatalytic water oxidation process, and it is incompatible with any air leak in the setup. The O_2 generated during the electrochemical experiment was expressed as the partial pressure of O_2. Hence, the number of moles of O_2 produced were calculated using the Ideal Gas Law as:

$$n_{O_2} = \frac{P_{O_2} \cdot V_{gs}}{R \cdot T}$$

where P_{O2} (atm) is the measured partial pressure of O_2, V_{gs} (L) is the volume of the gas space, R = 0.082 (atm L/K mol) is the ideal gas law constant and T = 298 K is the temperature.

The number of charges passed through the working electrode during the chronopotentiometry experiment was used to calculate the theoretical amount of O_2 produced as:

$$n_{O_2(theor)} = \frac{Q}{\nu_e F}$$

where Q (C) is the charge passed through the system, $\nu_e = 4$ is the number of electrons needed to generate one molecule of O_2 and F is the Faraday constant (96,485 C/mol).

Turnover frequency (TOF) estimation: The electrode pocket has a depth of 4 mm and a surface area of 0.07 cm^2. To calculate the TOFs a published method was followed, facilitating the determination of the mole quantities of the active catalyst.[17] Following this method, the volume of the carbon blend in the electrode pocket that is in contact with the aqueous solution is limited to 1/8 of the total volume. The penetration layer has a thickness of 0.5 mm. To calculate mole quantities of the POM in this volume, the weights of the electrodes were recorded before and after the introduction of the 30 wt.% Ba[POM]/CP blends. Considering the Ba[POM]/CP ratios and the molecular weight of the Ba[POMs], the total number of moles of Ba[POM] within each blend can be calculated. Finally, the mole quantities of active catalyst ($\mathbf{\Gamma}$ in Eq. 3; see main text) correspond to 1/8 of the total number of the mol quantities of Ba[POM].

		$Ba[Co_2Fe_2$-WS]	**$Ba[Co_4$-WS]**	**$Ba[Co_3W$-WS]**
Mass (g) of the electrode	Empty	3.33654	3.33655	3.33642
	Filled	3.38970	3.39220	3.39359
Molecular weight (g/mol)		6395.57	6101.42	6441.96
Total number of µmols		2.4936	2.7362	2.6624
$\mathbf{\Gamma}$ (µmols)		0.31170	0.34203	0.32799

4) Synthesis and Characterisation

All chemical and reagents were used as purchased without further purification. ALS, CPO Carbon Paste Oil was used to prepare carbon-paste modified electrodes.

Synthesis of $Na_{14}[Co^{II}_2(H_2O)_2Fe^{III}_2(B\text{-}\alpha\text{-}Co^{II}W_9O_{34})_2]\cdot 38H_2O$ ($Na[Co_2Fe_2\text{-}WS]$): The one-pot synthesis of the mixed metal cobalt-iron-containing Weakley sandwich POM was performed by reacting Co(II), Fe(III) and W(VI) in a 1:12.9:9.4 mole ratio at 80 °C. First, a 40 mL aqueous solution containing $Na_2WO_4\cdot 2H_2O$ (10.8g, 32 mmol) was heated at 80 °C (pH = 10.5). Separately, 3 mL of a supersaturated aqueous solution of sodium acetate was added to a solution of $Fe(NO_3)_3\cdot 9H_2O$ (1.8 g, 44 mmol) dissolved in 20 mL H_2O, which was then added to a solution of $Co(CH_3COO)_2\cdot 4H_2O$ (0.96 g, 3.4 mmol) dissolved in 15 mL of H_2O. The resulting solution was added dropwise to the above tungstate solution over a period of 30 minutes and the resulting mixture was kept at 80 °C. After one hour, the solution was filtered twice to remove a brown precipitate and the resulting filtrate (pH = 8.2) was left for crystallisation. Two types of olive-green crystals (rods and plates), both corresponding to **$Na[Co_2Fe_2\text{-}WS]$** started to appear after ca. one week. The crystals were collected by filtration and washed with water, then with methanol, and finally with acetone. The sample was dried in air. The yield of **$Na[Co_2Fe_2\text{-}WS]$** based on Co(II) was 18.7% (higher yields are achievable through extended crystallisation times and further evaporation of the solvent).

FT-IR data (in cm^{-1}): 917(m), 848(m), 692(m), 651(m), 440(w), 422(w) (Fig. S1). The counter cation content was determined by X-ray photoelectron spectroscopy (XPS) and EDX analyses (see Table S3 and Table S4). The constitutional H_2O content in the lattice was determined by thermogravimetric analysis (Fig. S2). PXRD patterns of the sample and comparison with the single crystal data, confirm the structural identity of rod- and plate-shaped crystals (Fig. S3). EDX analysis (atomic %): Expected: W, 47.37; Co, 10.53; Fe, 5.26; Na, 36.84; Found: W, 47.48, Co, 10.72; Fe, 5.39; Na, 36.41. M_w = 5787.15 g mol^{-1}.

Preparation of $Ba_{6.7}Na_{0.6}[Co^{II}_2(H_2O)_2Fe^{III}_2(B\text{-}\alpha\text{-}Co^{II}W_9O_{34})_2]\cdot 37.8H_2O$ ($Ba[Co_2Fe_2\text{-}WS]$): To a solution of 0.20 g of **$Na[Co_2Fe_2\text{-}WS]$** in 20 mL of H_2O, solid $BaCl_2$ was slowly added while stirring until precipitation of a pale olive green solid corresponding to **$Ba[Co_2Fe_2\text{-}WS]$** was completed, leaving a colourless solution. The precipitate was filtered under vacuum and washed with water and acetone and dried in air.

The FT-IR and Raman spectra are identical to those obtained for **$Na[Co_2Fe_2\text{-}WS]$** (see Fig. S1 and Fig. S4). The countercation content was determined by X-ray photoelectron spectroscopy (XPS) and EDX analyses (see Table S3 and Table S4). The constitutional H_2O content in the lattice was determined by thermogravimetric analysis (Fig. S5). EDX analysis (atomic %): Expected: W, 57.75; Co, 12.78; Fe, 6.39; Na, 1.92; Ba, 21.41; Found: W, 57.75, Co, 12.54; Fe, 6.79; Na, 2.16; Ba, 20.76. M_w = 6395.57 g mol^{-1}.

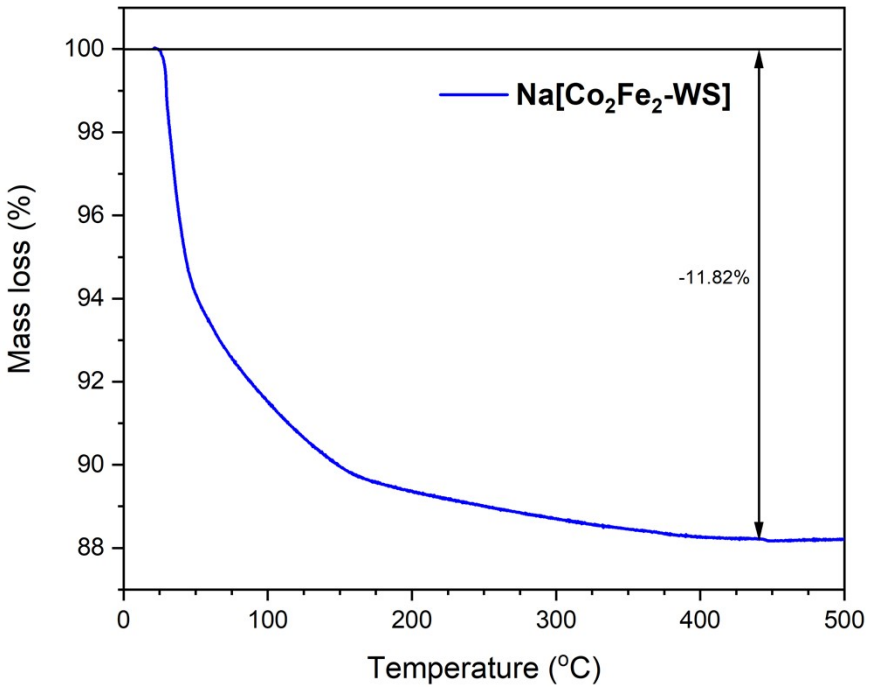

Fig. S1: FT-IR spectra of $Na_{14}[Co^{II}_2(H_2O)_2Fe^{III}_2(B\text{-}\alpha\text{-}Co^{II}W_9O_{34})_2]\cdot 38H_2O$ (**Na[Co_2Fe_2-WS]**, blue) and $Ba_{6.7}Na_{0.6}[Co^{II}_2(H_2O)_2Fe^{III}_2(B\text{-}\alpha\text{-}Co^{II}W_9O_{34})_2]\cdot 37.8H_2O$ (**Ba[Co_2Fe_2-WS]**, red).

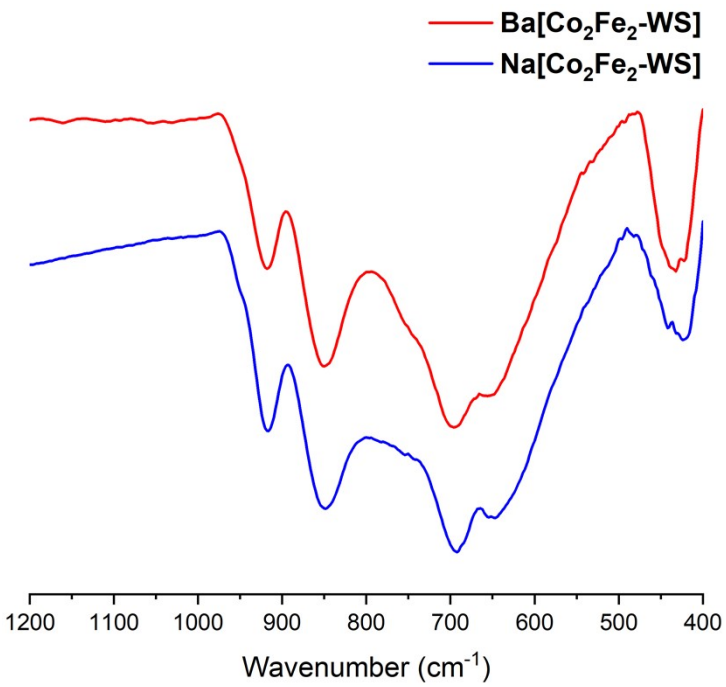

Fig. S2: Thermogravimetric analysis for $Na_{14}[Co^{II}_2(H_2O)_2Fe^{III}_2(B\text{-}\alpha\text{-}Co^{II}W_9O_{34})_2]\cdot 38H_2O$ (**Na[Co_2Fe_2-WS]**).

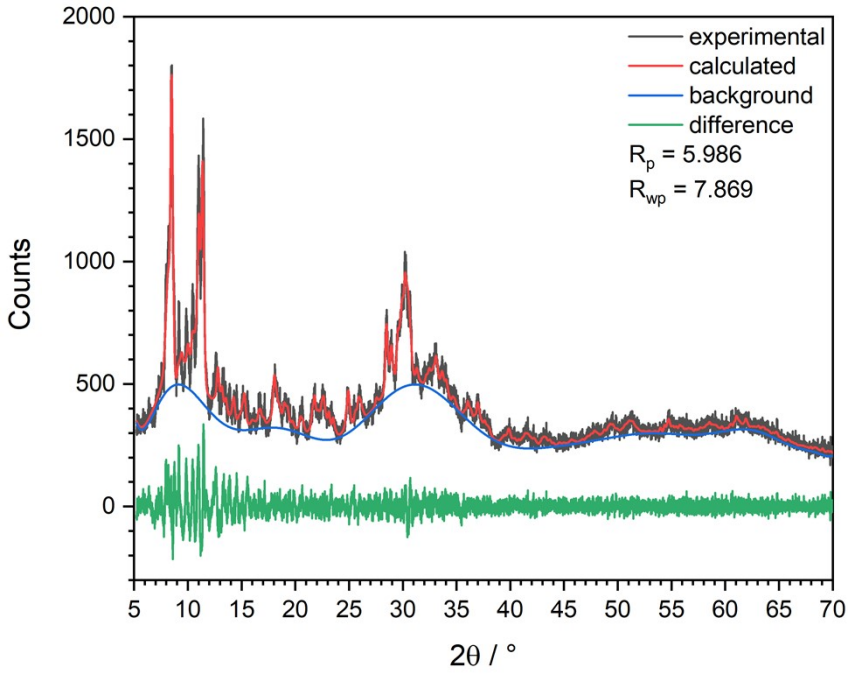

Fig. S3: PXRD pattern for $Na_{14}[Co^{II}_2(H_2O)_2Fe^{III}_2(B\text{-}\alpha\text{-}Co^{II}W_9O_{34})_2]\cdot 38H_2O$ (**Na[Co_2Fe_2-WS]**, black) compared to a simulated pattern based on single crystal data (red).

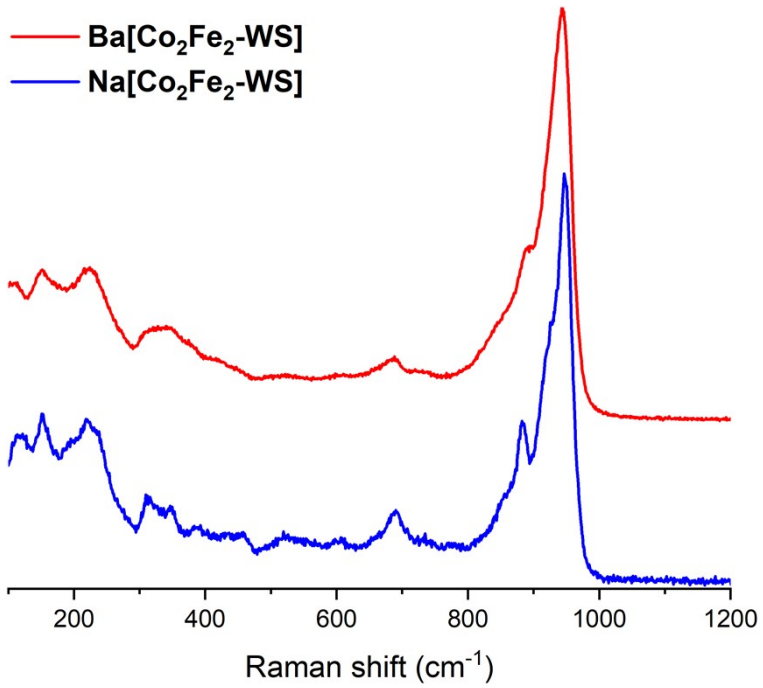

Fig. S4: Raman spectra for $Na_{14}[Co^{II}_2(H_2O)_2Fe^{III}_2(B\text{-}\alpha\text{-}Co^{II}W_9O_{34})_2]\cdot 38H_2O$ (**Na[Co_2Fe_2-WS]**, blue) and $Ba_{6.7}Na_{0.6}[Co^{II}_2(H_2O)_2Fe^{III}_2(B\text{-}\alpha\text{-}Co^{II}W_9O_{34})_2]\cdot 37.8H_2O$ (**Ba[Co_2Fe_2-WS]**, red).

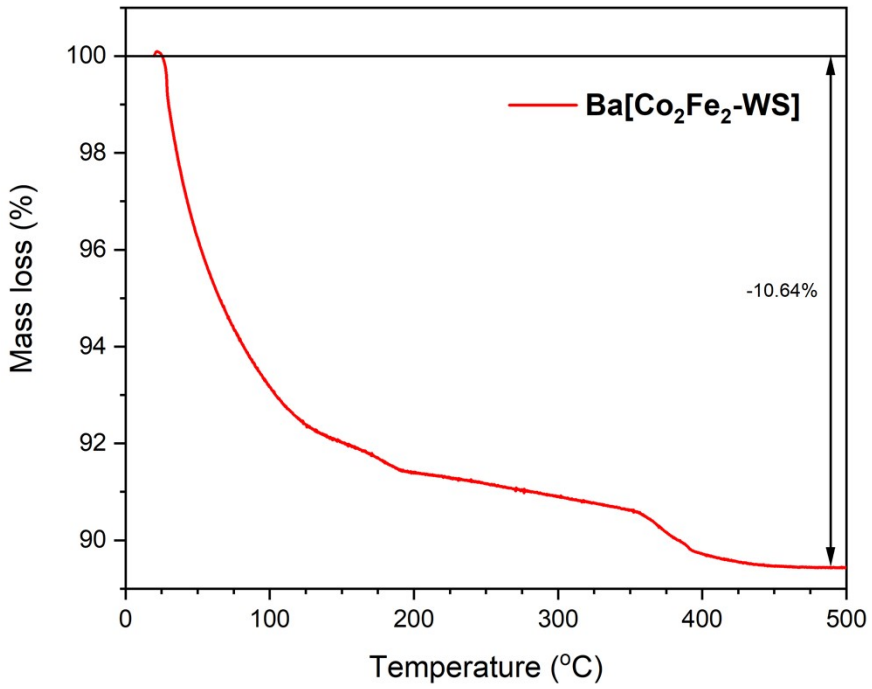

Fig. S5: Thermogravimetric analysis for $Ba_{6.7}Na_{0.6}[Co^{II}_2(H_2O)_2Fe^{III}_2(B\text{-}\alpha\text{-}Co^{II}W_9O_{34})_2]\cdot 37.8H_2O$ (**$Ba[Co_2Fe_2\text{-}WS]$**).

Synthesis of $Na_{12}[Co^{II}_2(H_2O)_2Co^{II}W^{VI}(B\text{-}\alpha\text{-}Co^{II}W_9O_{34})_2]\cdot 44.3H_2O$ ($Na[Co_3W\text{-}WS]$): $Na_2WO_4\cdot 2H_2O$ (56.0 g, 170 mmol) was dissolved in 250 mL of H_2O and the pH was adjusted to 7.5 with glacial acetic acid. This solution was heated at 80 °C under stirring. Separately, $Co(CH_3COO)_2\cdot 4H_2O$ (7.0 g, 28.1 mmol) was dissolved in 100 mL of H_2O and added to a 100 mL aqueous solution containing $Co(NO_3)_2\cdot 6H_2O$ (7.0 g, 14 mmol), yielding a purple solution. The latter solution was added dropwise to the tungstate solution slowly yielding a teal-coloured solution. After complete addition, the solution was heated at reflux for one hour, cooled to room temperature and filtered repeatedly to remove a teal precipitate. The solution (pH = 6.3) was left to crystallise. After two weeks water-insoluble pink crystals appeared, which unfortunately were not suitable for single crystal X-ray measurements. The mixture was filtered and left to crystallize. After two additional weeks, further pink crystals appeared together with emerald-green needle-shaped crystals. The emerald-green needles were decanted from the mother liquor, dissolved with H_2O and separated from the pink crystals by filtration. Sodium acetate (1 g) was added to the resulting green solution, filtered again, and left to crystallise. After one day, pure emerald-green needles (**$Na[Co_3W\text{-}WS]$**) were obtained, collected by filtration, washed with water, methanol, and acetone. The pure sample was dried in air. The mother liquor was also left to crystallize, which continued yielding pink and emerald-green crystals. The previously described procedure was repeated to obtain a phase-pure sample of **$Na[Co_3W\text{-}WS]$** crystals (Yield based on Co: *ca.* 2 %)

FT-IR data (in cm^{-1}): 915(m), 861(m), 725(br), 688(m), 644(m), 531(w), 419(w) (Fig. S6). Water content was determined by TGA (Fig. S7). EDX analysis (atomic %): Expected: W, 52.78; Co, 13.89; Na, 33.33; Found: W, 51.59, Co, 12.06; Na, 36.34. M_w = 5985.76 g mol^{-1}.

Preparation of $Ba_6[Co^{II}_2(H_2O)_2Co^{II}W^{VI}(B\text{-}\alpha\text{-}Co^{II}W_9O_{34})_2]\cdot 39.2H_2O$ ($Ba[Co_3W\text{-}WS]$): The preparation of the title compound was performed following the same procedure as described for **$Ba[Co_2Fe_2\text{-}WS]$**.

The FT-IR spectrum is identical to that obtained for **Na[Co$_3$W-WS]** (see Fig. S6). The countercation content was determined by EDX spectroscopy. The constitutional H_2O content was determined by TGA (Fig. S8). EDX analysis (atomic %): Expected: W, 63.33; Co, 16.67; Ba, 20.00; Found: W, 64.51, Co, 14.57; Ba, 20.93. M_w = 6441.96 g mol^{-1}.

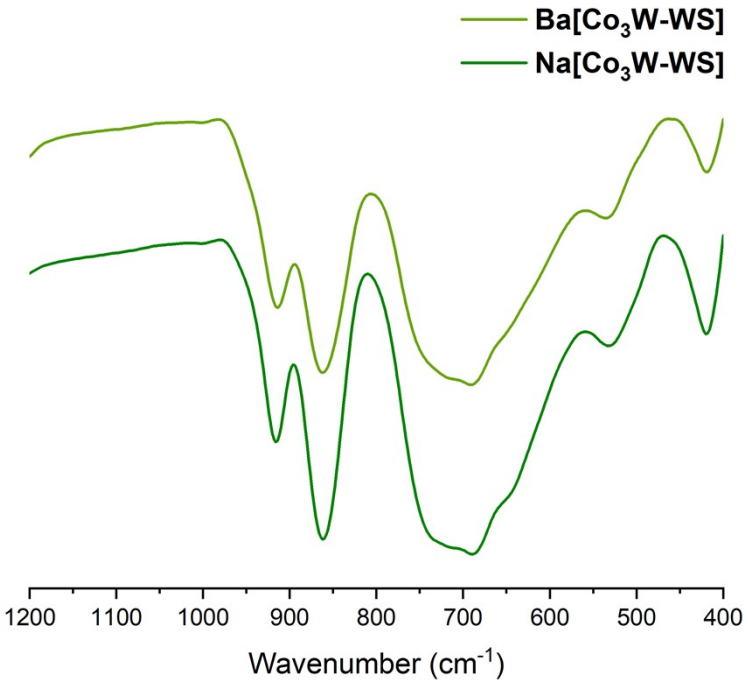

Fig. S6: FT-IR spectra of $Na_{12}[Co^{II}_2(H_2O)_2Co^{II}W^{VI}(B\text{-}\alpha\text{-}Co^{II}W_9O_{34})_2]\cdot 44.3H_2O$ (**Na[Co$_3$W-WS]**, dark green) and $Ba_6[Co^{II}_2(H_2O)_2Co^{II}W^{VI}(B\text{-}\alpha\text{-}Co^{II}W_9O_{34})_2]\cdot 39.2H_2O$ (**Ba[Co$_3$W-WS]**, light green).

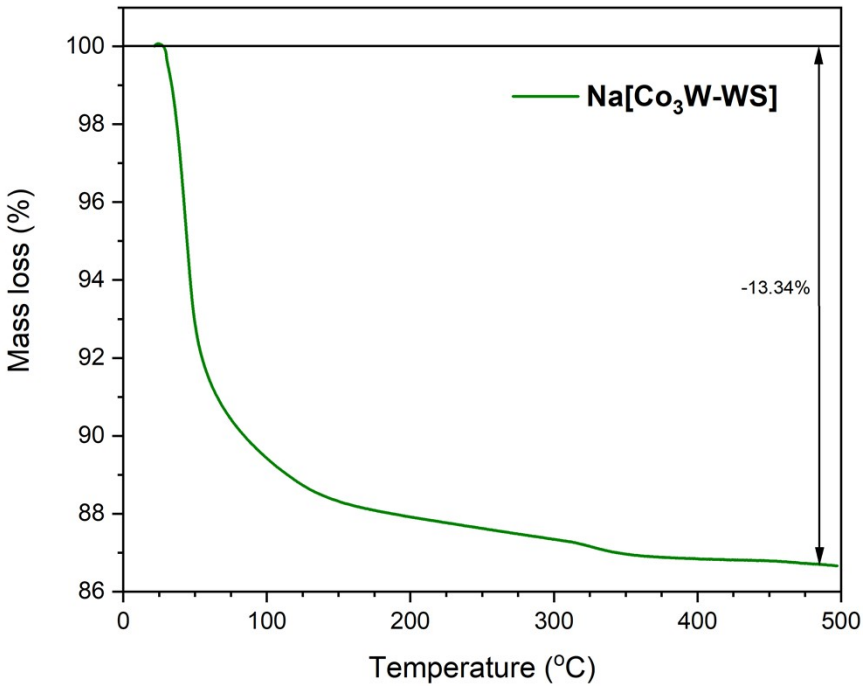

Fig. S7: Thermogravimetric analysis for $Na_{12}[Co^{II}_2(H_2O)_2Co^{II}W^{VI}(B\text{-}\alpha\text{-}Co^{II}W_9O_{34})_2]\cdot 44.3H_2O$ (**Na[Co$_3$W-WS]**).

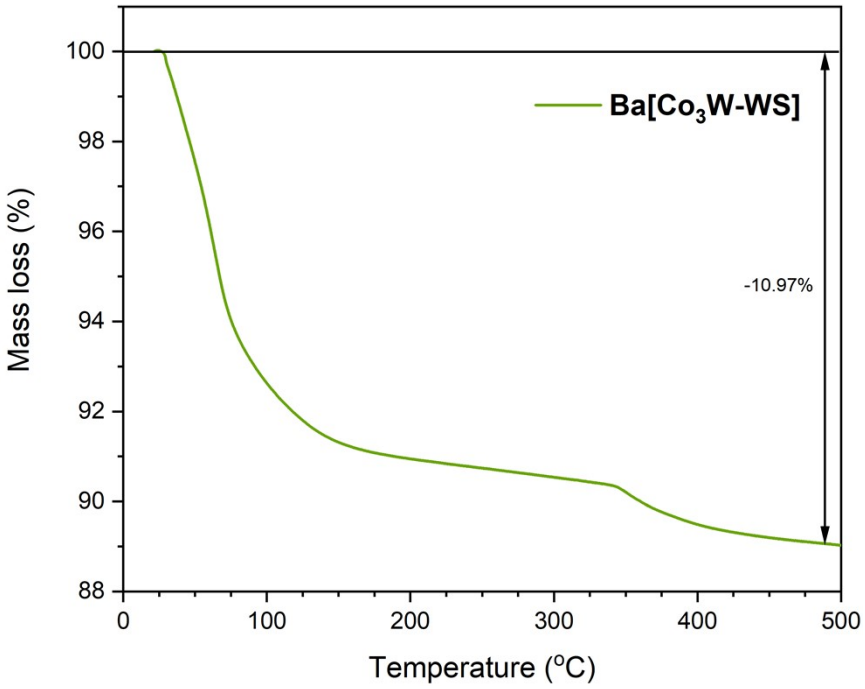

Fig. S8: Thermogravimetric analysis for $Ba_6[Co^{II}_2(H_2O)_2Co^{II}W^{VI}(B\text{-}\alpha\text{-}Co^{II}W_9O_{34})_2]\cdot 39.2H_2O$ (**Ba[Co_3W-WS]**).

Synthesis of $K_{10}[Co^{II}_2(H_2O)_2Co^{II}_2(B\text{-}\alpha\text{-}PW_9O_{34})_2]$ (K[Co_4-WS]): This well-known polyoxometalate was prepared applying an optimised literature method.[18] $Na_2WO_4\cdot 2H_2O$ (33.0 g, 100 mmol) and Na_2HPO_4 (1.57 g, 11.1 mmol) were dissolved in 100 mL of H_2O and the pH was adjusted to 6.5 through addition of glacial acetic acid. To this mixture, a solution containing of $Co(CH_3COO)_2\cdot 4H_2O$ (5.48 g, 22 mmol) in 50 mL of H_2O, was added. The resulting dark-purple solution was refluxed for 2 hours. After this time period the mixture was filtered twice to remove a residual purple precipitate. The resulting solution was saturated with 3 g of potassium acetate, filtered again, and allowed to cool at room temperature. Rhombic, purple crystals of **K[Co_4-WS]** were collected by filtration, washed with water, methanol, and acetone. The sample was dried in air.

The compound was characterised by FT-IR spectroscopy (Fig. S9).

Preparation of $Ba_5[Co^{II}_2(H_2O)_2Co^{II}_2(B\text{-}\alpha\text{-}PW_9O_{34})_2]\cdot 38H_2O$ (Ba[Co_4-WS]): The preparation of **Ba[Co_4-WS]** was achieved by metathesis reaction following an established literature method.[19]

The FT-IR spectrum is identical to that obtained for **K[Co_4-WS]** (see Fig. S9). The countercation content was determined by EDX analysis. EDX analysis (atomic %): Expected: W, 62.07; Co, 13.79; P, 6.90; Ba, 17.24; Found: W, 65.14, Co, 12.56; P, 4.50; Ba, 17.81. M_w = 6101.42 g mol^{-1}.

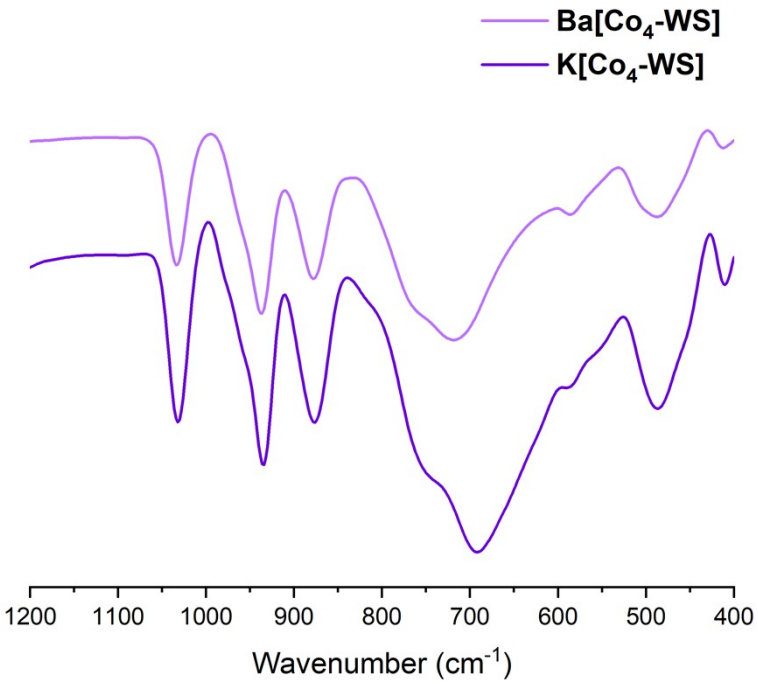

Fig. S9: FT-IR spectra of $K_{10}[Co^{II}_2(H_2O)_2Co^{II}_2(B\text{-}\alpha\text{-}PW_9O_{34})_2]$ (**K[Co_4-WS]**, purple) and $Ba_5[Co^{II}_2(H_2O)_2Co^{II}_2(B\text{-}\alpha\text{-}PW_9O_{34})_2]\cdot 38H_2O$ (**Ba[Co_4-WS]**, dark purple).

5) Crystallographic Data

Crystals description:

The olive-green rod-shaped crystals (**Na[Co_2Fe_2-WS]_rods**) were solved and refined in the triclinic space group $P\bar{1}$, whereby half of a cluster entity is located in the asymmetric unit. The following cell parameters were determined: *a* = 12.2859(6) Å, *b* = 13.6630(6) Å, *c* = 14.9308(6) Å, *α* = 99.3780(10)°, *β* = 104.1870(10)°, *γ* = 101.318(2)°, *V* ~ 2,323 Å^3. In the solid state, the Co^{II} heteroatom within the {B-α-$Co^{II}W_9O_{34}$} unit has a distorted tetrahedral geometry, characterised by Co^{II}–O bond lengths varying between 1.886(8) – 1.911(8) Å, and O–Co^{II}–O angles varying between 105.7(4) – 113.4(4)°. The Co^{II} and Fe^{III} atoms placed at the central oxo belt have a distorted octahedral geometry. The Co^{II}–O bond lengths and O–Co^{II}–O angles involving adjacent O-donor atoms, vary in the range of 2.005(8) – 2.160(8) Å and 82.7(3) – 96.4(3)°, respectively, whereas the corresponding Fe^{III}–O bond lengths and O–Fe^{III}–O angles deviate between 2.009(8) – 2.141(9) Å and 81.0(4) – 94.8(3)°, respectively.

Olive-green plate-shaped crystals (**Na[Co_2Fe_2-WS]_plates**) could also be identified in the reaction mixture. These crystals were of lower quality. Initial diffraction studies substantiated that the plate-shaped crystals were severely twinned crystals. A structure refinement of multiple-twinned crystals was achieved in the orthorhombic crystal system in the space group *P*ccn. The measurement confirmed that the compound consists of an isostructural polyoxometalate cluster core to **Na[Co_2Fe_2-WS]_rods**. The H-atoms of the constitutional solvent molecules were not located and refined.

When a mixture of the two types of crystals, **Na[Co_2Fe_2-WS]_rods** and **Na[Co_2Fe_2-WS]_plates,** was dissolved in H_2O and recrystallised upon addition of sodium acetate, phase-pure, block-shaped crystals were obtained after approximately 4 weeks. These olive-green, block-shaped crystals were suitable for single-crystal X-ray measurements. The data analysis confirmed that the structure corresponds to that of the title compound (**Na[Co_2Fe_2-WS]_recrystallised**), thus indicating that the integrity of molecular POM structure is maintained in solution. The data was solved and refined in the orthorhombic space group *Pccn*. Half of a cluster entity is located in the asymmetric unit which reflects the C_{2h} symmetry of the molecule. The following cell parameters were determined: *a* = 21.063(2) Å, *b* = 26.187(2) Å, *c* = 17.8488(19) Å, *α* = *β* = *γ* = 90°, *V* ~ 9,845 Å^3. In this crystal structure, the tetrahedral Co^{II} heteroatom in the {B-α-$Co^{II}W_9O_{34}$} unit gives rise to Co^{II}–O bond lengths varying between 1.865(14) – 1.884(13) Å, and O–Co^{II}–O angles involving adjacent O-donor atoms, deviated between 106.1(5) – 112.2(6)°. The octahedrally coordinated Co^{II} and Fe^{III} ions located in the central oxo belt have Co^{II}–O bond lengths and O–Co^{II}–O angles, varying between 2.028(12) – 2.139(13) Å and 82.4(5) – 99.5(6)°, respectively. The Fe^{III}–O bond lengths and O–Fe^{III}–O angles range between 2.002(14) – 2.137(13) Å and 80.4(5) – 95.2(5)°, respectively.

Whilst **Na[Co_2Fe_2-WS]_rods** and **Na[Co_2Fe_2-WS]_recrystallised** have almost identical cluster cores, the arrangement/number of constitutional solvent water molecules and the arrangement of counterions differ, which is further reflected in different packing arrangements. The H-atoms of the constitutional solvent molecules were not located and refined.

Table S1: Crystallographic data and structure refinement for **Na[Co_2Fe_2-WS]_rods**, **Na[Co_2Fe_2-WS]_plates**, **Na[Co_2Fe_2-WS]_recrystallised** and **Na[Co_3W-WS]**.

Name	Na[Co_2Fe_2-WS]_rods	Na[Co_2Fe_2-WS]_plates	Na[Co_2Fe_2-WS]_recrystalised	Na[Co_3W-WS]
CSD No.	**2068500**	**2068501**	**2068065**	**2068502**
Empirical formula	$Co_4Fe_2H_{75}Na_{14}O_{105.5}W_{18}$	$Co_4Fe_2H_{62}Na_{14}O_{101}W_{18}$	$Co_4Fe_2H_{92}Na_{14}O_{116}W_{18}$	$Co_5H_{82}Na_{12}O_{109}W_{19}$
Formula weight (g/mol)	5741.93	5656.83	5927.06	5890.08
Temperature/K	100(2)	100(2)	100(2)	100(2)
Crystal system	triclinic	orthorhombic	orthorhombic	monoclinic
Space group	P-1	Pccn	Pccn	$P12_1/n1$
a (Å)	12.2859(6)	20.9875(19)	21.063(2)	13.063(11)
b (Å)	13.6630(6)	26.045(2)	26.187(2)	17.764(15)
c (Å)	14.9308(6)	17.7454(16)	17.8488(19)	21.118(18)
α (deg)	99.3780(10)	90	90	90
β (deg)	104.1870(10)	90	90	93.152(9)
γ (deg)	101.318(2)	90	90	90
Volume (Å^3)	2323.17(18)	9700.1(15)	9845.2(16)	4893(7)
Z	1	4	4	2
ρ_{calc} (g/cm^3)	4.087	3.831	3.968	3.942
Absorption coefficient (mm^{-1})	23.369	22.380	22.063	23.232
F(000)	2541	9816	10576	5090
crystal size (mm^3)	0.276 × 0.097 × 0.048	0.252 × 0.199 × 0.114	0.180 × 0.160 × 0.130	0.200 × 0.070 × 0.050
Radiation	MoKα (λ = 0.71073)	MoKα (λ = 0.71073)	MoKα (λ = 0.71073)	MoKα (λ = 0.71073)
2Θ range for data collection (deg)	3.118 to 66.402	2.492 to 50.700	2.482 to 52.742	2.998 to 59.248
Index ranges	-9 ≤ h ≤ 18, -21 ≤ k ≤ 21, -22 ≤ l ≤ 22	-25 ≤ h ≤ 24, -31 ≤ k ≤ 31, -21 ≤ l ≤ 17	-26 ≤ h ≤26, -32 ≤ k ≤ 32, -22 ≤ l ≤ 22	-18 ≤ h ≤18, -21 ≤ k ≤ 24, -29 ≤ l ≤ 28
no. of reflections collected	54956	93207	246675	46062
no. of independent reflections	17691 [R_{int} = 0.0627, R_{sigma} = 0.0736]	8884 [R_{int} = 0.1017, R_{sigma} = 0.0419]	10071 [R_{int} = 0.1106, R_{sigma} = 0.0353]	13682 [R_{int} = 0.1017, R_{sigma} = 0.1182]
Data/restraints/parameters	17691/30/692	8884/917/636	10071/354/688	13682/102/676
Goodness-of-fit on F²	1.058	1.117	1.199	1.019
Final R indexes[a] [I>=2σ (I)]	R_1 = 0.0570, wR_2 = 0.1250	R_1 = 0. 1045, wR_2 = 0.3121		R_1 = 0.0570, wR_2 = 0.1003
Final R indexes [all data]	R_1 = 0.0950, wR_2 = 0.1462	R_1 = 0.1333, wR_2 = 0.3337	R_1 = 0.0819, wR_2 = 0.1216	R_1 = 0.1152, wR_2 = 0.1167
Largest diff. peak/hole / e Å^{-3}	5.598/-5.698	4.756/-2.695	4.554/-2.978	3.866/-3.246

[a] $R_1 = \Sigma||F_o| - |F_c|| / \Sigma|F_o|$; $wR_2 = \Sigma[w(F_o^2 - F_c^2)^2] / \Sigma[w(F_o^2)^2]^{1/2}$

Table S2: Bond Valence Sum (BVS) analysis of the cobalt and iron atoms in **Na[Co_2Fe_2-WS]_rods** and **Na[Co_2Fe_2-WS]_recrystallised**.

Compound	Atom	Bond Valence Sum
Na[Co_2Fe_2-WS]_rods	Co1	2.299
	Co2	2.055
	Fe1	2.683
Na[Co_2Fe_2-WS]_plates	Co1	2.054
	Co2	2.355
	Fe1	2.689
Na[Co_2Fe_2-WS]_recrystalised	Co1	2.461
	Co2	2.094
	Fe1	2.737

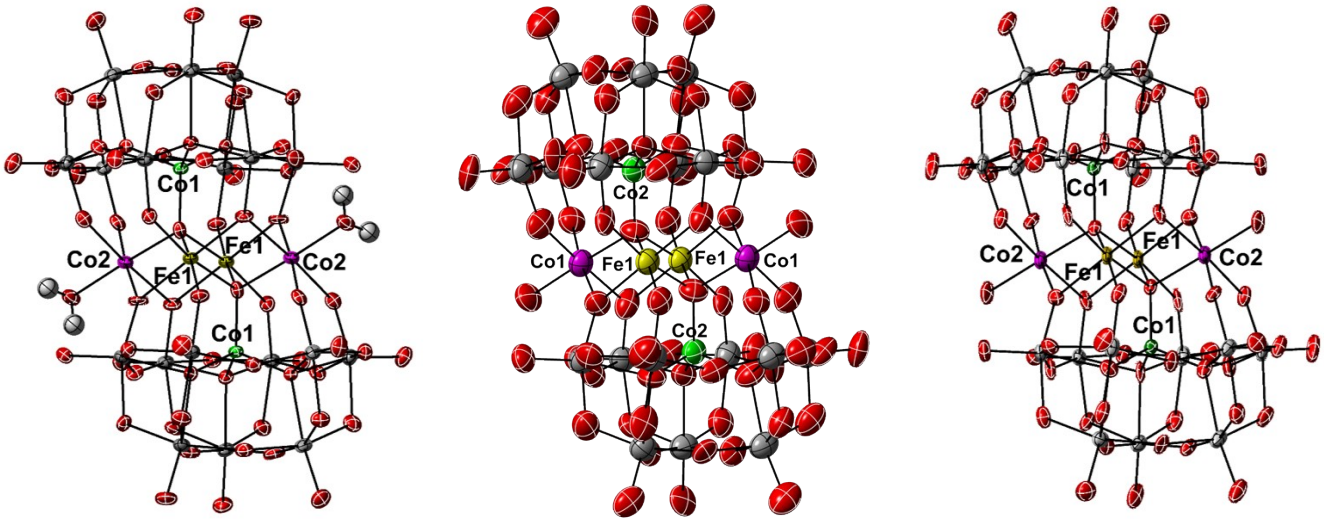

Fig. S10: Ellipsoid representation of the refined crystal structures for **Na[Co_2Fe_2-WS]_rods** (left), **Na[Co_2Fe_2-WS]_plates** (center) and **Na[Co_2Fe_2-WS]_recrystallised** (right). Colour code: Co (octahedral): pink; Co (tetrahedral): green; Fe: yellow; W: grey; O: red; H: white.

6) Magnetic properties

Anisotropic Exchange Model and thermal dependence of χT:

The distorted octahedral Co^{II} ion presents a $^4T_1$ high-spin ground state that with a first-order spin-orbit coupling unfolds into six anisotropic Kramers doublets. Only the lowest doublet can be considered in the model as a highly anisotropic effective spin 1/2. For the case of tetrahedral Co^{II} and octahedral Fe^{III} ions, the ground state can be considered a spin only 3/2 and 5/3, respectively. Considering all these aspects and the exchange network scheme for **$Na[Co_2Fe_2$-WS]** when the two iron ions occupy the short diagonal of the rhombus, the effective exchange Hamiltonian can be written as:

$$\hat{H} = -2J_{12}\hat{S}_1\hat{S}_2 - 2\sum_{\alpha=x,y,z}\sum_{i=1,2}\sum_{j=3,4} J_{13}^{\alpha}\hat{S}_i^{\alpha}\hat{S}_j^{\alpha} - 2\sum_{\alpha=x,y,z}\sum_{i=1,2}\sum_{j=5,6} J_{15}^{\alpha}\hat{S}_i^{\alpha}\hat{S}_j^{\alpha} - 2\sum_{\alpha=x,y,z} J_{35}^{\alpha}\left(\hat{S}_3\hat{S}_5 + \hat{S}_4\hat{S}_6\right)$$

where J_{12} is the isotropic interaction between both Fe^{III} centres, J_{13} and J_{15} are the anisotropic interactions between Fe^{III} ions and tetrahedral and octahedral Co^{II} ions, respectively, and J_{35} are the anisotropic interaction between both types of cobalt atoms.

The Zeeman interaction terms have been considered in the effective Hamiltonian: Isotropic for the irons and tetrahedral the cobalts with a Landé factors, g, equal to 2, and anisotropic for the octahedral cobalt with an average value of g equal to 4.33 for the effective spin 1/2. This anisotropy of g marks the exchange anisotropy, in such a way that the exchange parameters between two centers are proportional to the product of the individual g of each center. Therefore, with only the anisotropy parameter for the Landé factor of the octahedral cobalt, the anisotropy in the different exchange parameters can be defined. For the same anisotropy in g, the exchange between octahedral cobalt ions will be much greater than the other anisotropic exchange interactions (Fe – Co_{Oh} or Co_{Oh} – Co_{Td}).

To find regions of the parameters that could reproduce the experimental properties, the entire parameter space has been explored. The exchange interaction between the iron centres has been set at -2.75 cm^{-1}, which is the value obtained for other similar polyanions,[20] and the exchange interaction between cobalt ions of different coordination index has been set to -10 cm^{-1}, similar value to that obtained by INS.[21–23] Figure S11 shows the fundamental spin as a function of the two exchange parameters between the iron ions and the two types of cobalt ions (J_{13} tetrahedral and J_{15} octahedral). The contour plot figure shows the fundamental spin when the exchange interactions become isotropic. This limiting case helps to understand which parameter regions may be compatible with the experimental data. In fact, the regions that give temperature susceptibility product curves correspond in this contour plot to regions where S=1 is the fundamental close to S=3 at the bottom right or top left. Susceptibility curves for one case from each of these regions are also shown. The different lines correspond to different values of anisotropy of g of the octahedral cobalt ion (from Ising case to isotropic). We see in the first two figures that they are quite compatible with the experimental measurements. However, in the third case presented, which corresponds to a region where S=1 is very stable, the susceptibility curves no longer reproduce the experimental values. Regions with high fundamental spin present in the χT curve maximums at low temperature and therefore

also incompatible with the experimental results. We can conclude that there are two broad regions of parameters where the magnetic properties can be compatible with the experimental ones.

A similar study has been carried out for the case of the two cobalt ions placed at the two inner octahedral, coordinatively saturated positions of the rhombus, but no regions have been found where we can ensure that they

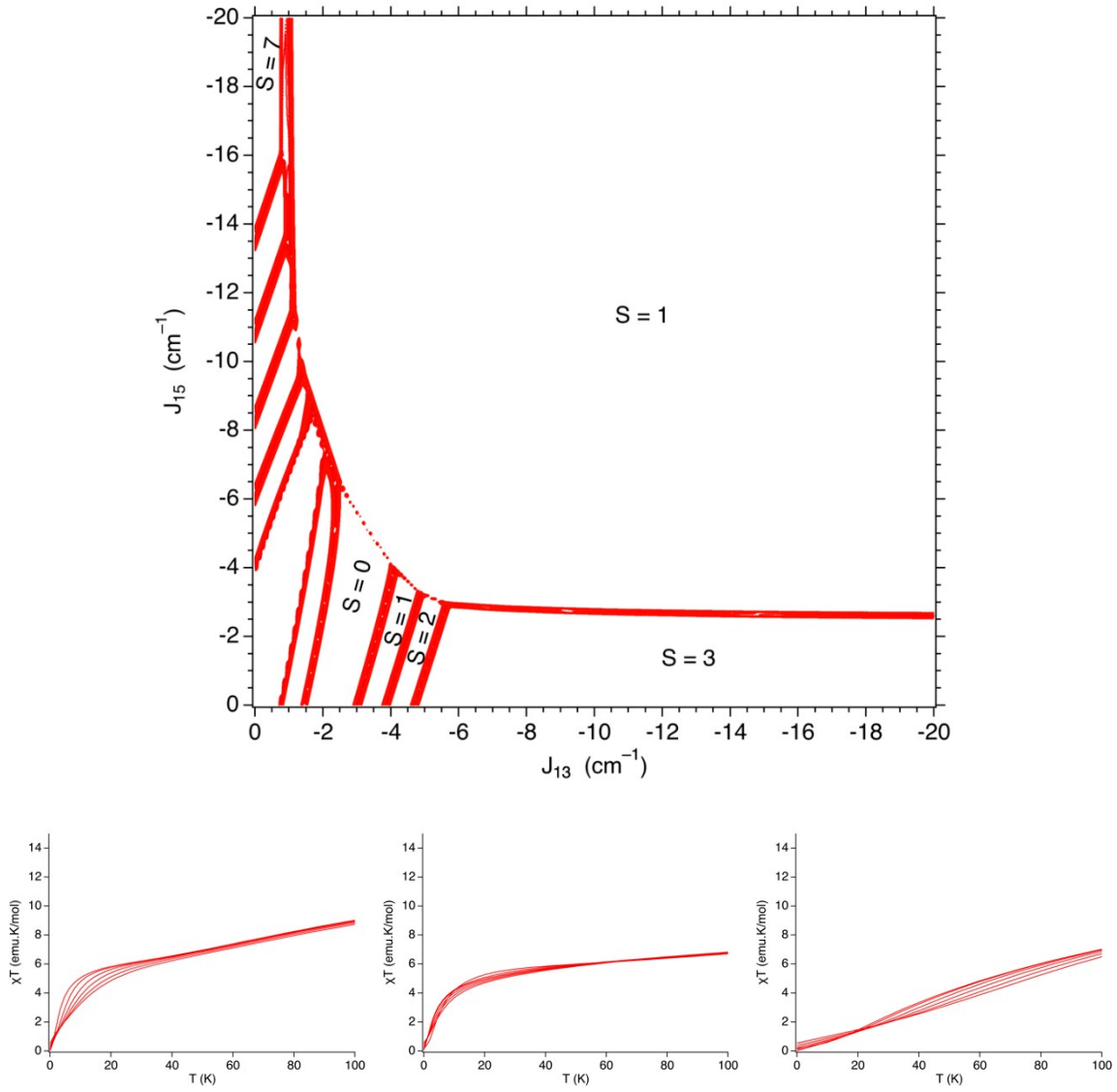

reproduce the experimental magnetic properties.

Fig. S11: (Top) Distribution of the fundamental spin as a function of the two exchange interactions between iron and each type of cobalt (J_{13} for tetrahedral and J_{15} for octahedral) for **Na[Co_2Fe_2-WS]** with iron ions placed at the short diagonal of central rhombus. (Down) Thermal dependence of the product χT for different axial anisotropy in region with: (left) the Fe^{III}-Co^{II}_{Oh} interaction being more negative than -10 cm^{-1} and the Fe^{III}-Co^{II}_{Td} interaction being around -1.2 cm^{-1}; (center) the Fe^{III}-Co^{II}_{Oh} interaction being around -3.2 cm^{-1} and the Fe^{III}-Co^{II}_{Td} interaction being more negative than -6 cm^{-1}; (right) and the central part of the contour plot with both parameters of similar magnitude.

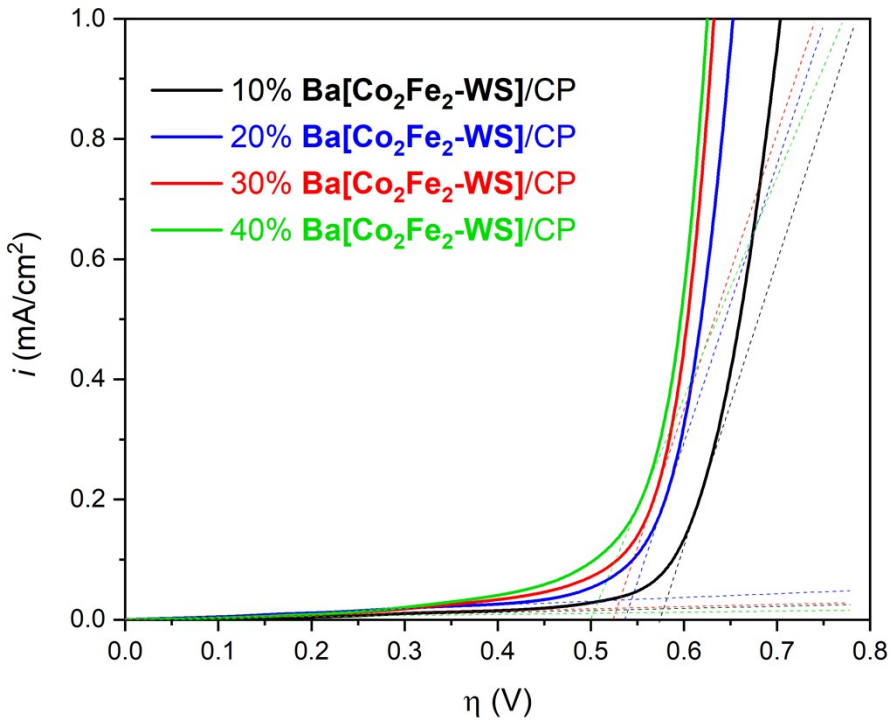

7) Electrochemistry and Post-catalytic Characterisation

Fig. S12: OER onset overpotential determination using variable quantities of **Ba[Co_2Fe_2-WS]** in the carbon blend (KP_i buffer at pH = 7.2). The determined values are: 577 mV for 10 wt.%, 543 mV for 20 wt.%, 528 mV for 30 wt.% and 502 mV for 40 wt.%.

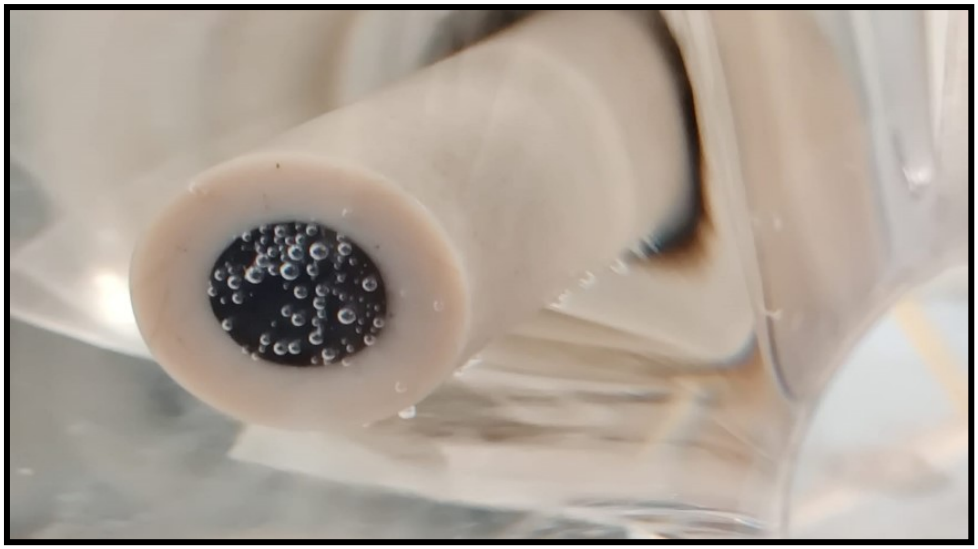

Fig. S13: Optical image of a **Ba[Co_2Fe_2-WS]**/CP electrode during bulk water electrolysis showing the evolved O_2 bubbles that are attached to the surface of the electrode.

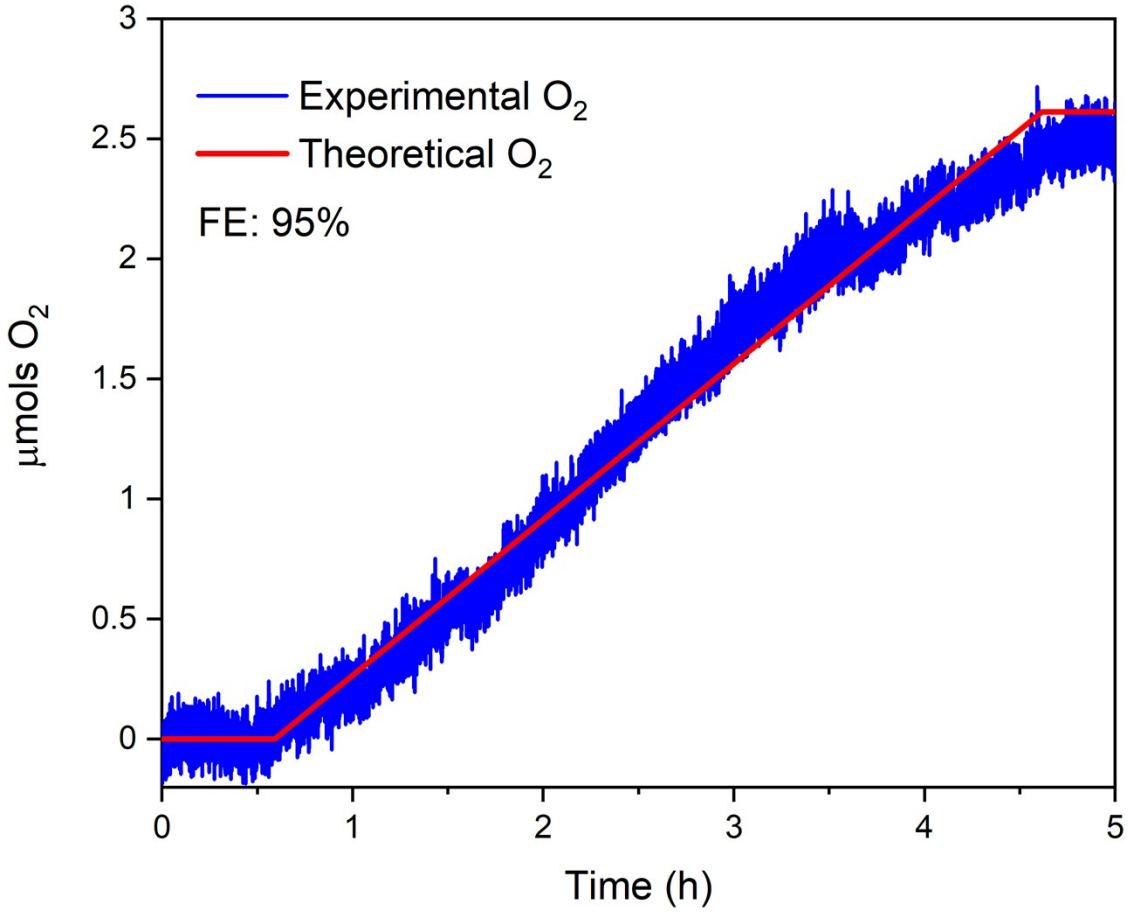

Fig. S14: Measurement of the O_2 evolved during a chronopotentiometry at 1 mA/cm^2 employing a 30 wt.% **Ba[Co_2Fe_2-WS]**/CP electrode. The experiment was conducted in a two-neck round bottom flask (50 mL) using a pH 7.2, 50 mM KP_i buffer and KNO3 (1M) as electrolyte.

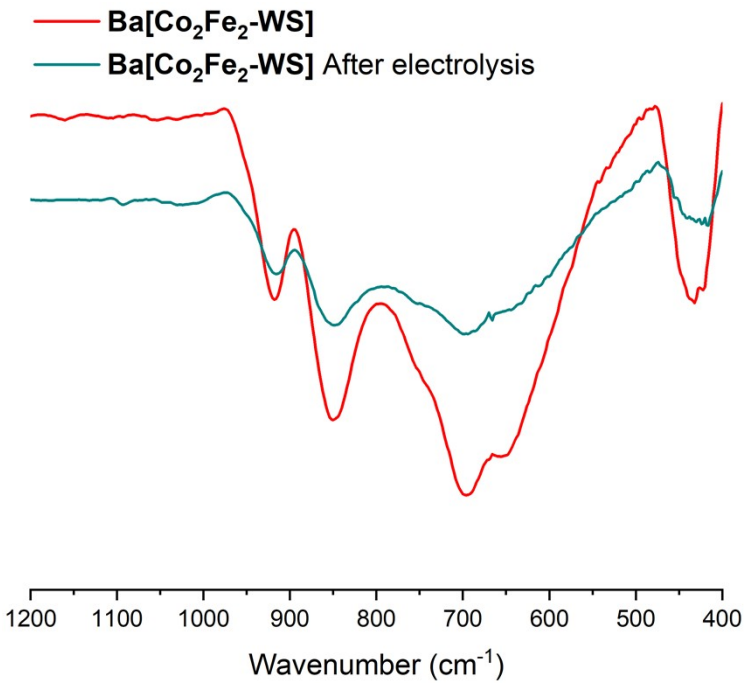

Fig. S15: FT-IR spectra of **Ba[Co_2Fe_2-WS]** as prepared (red), and **Ba[Co_2Fe_2-WS]** recovered (dark cyan) from the carbon paste blend after 18 hours of bulk water electrolysis at 1 mA/cm^2 in a KP_i buffer at pH = 7.2.

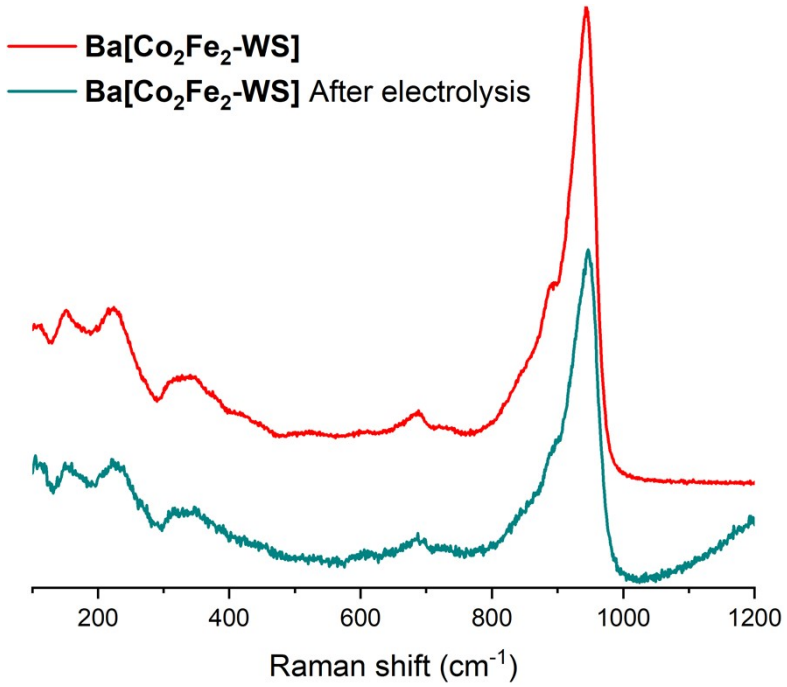

Fig. S16: Raman spectra of **Ba[Co_2Fe_2-WS]** as prepared (red), and **Ba[Co_2Fe_2-WS]** recovered (dark cyan) from the carbon paste blend after 18 hours of bulk water electrolysis at 1 mA/cm^2 in a KP_i buffer at pH = 7.2.

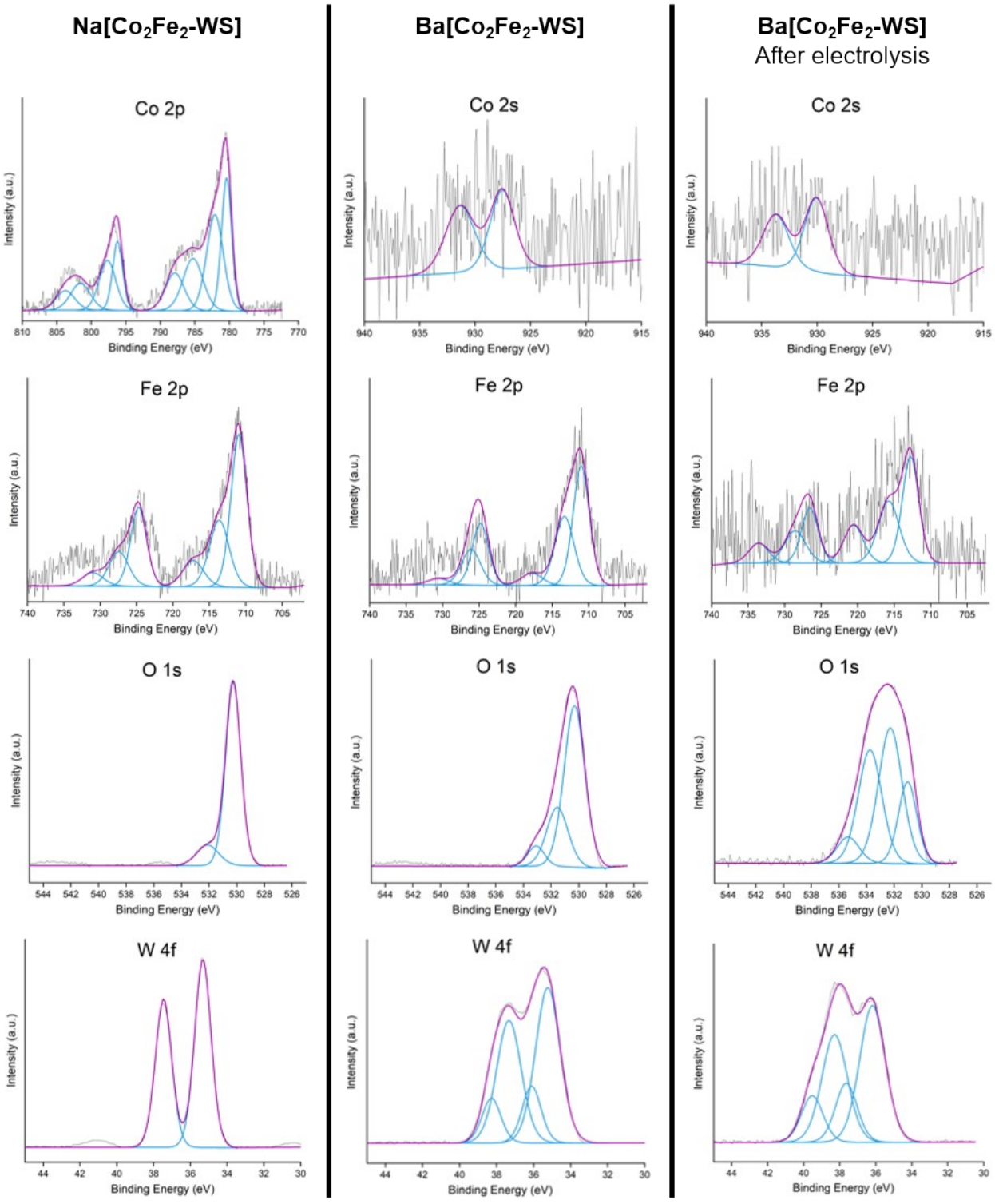

Fig. S17: XPS data (Co, Fe, O and W edges) for **Na[Co_2Fe_2-WS]**, and **Ba[Co_2Fe_2-WS]** as prepared and recovered from the carbon paste blend after 18 hours of bulk water electrolysis at 1 mA/cm^2 in a KP_i buffer at pH = 7.2. Due to the strong overlap between the Ba3d and Co2p edges, we compared the Co2s edges for **Ba[Co_2Fe_2-WS]**. There are no signals that can be assigned to CoO_x formed under working conditions. The O1s signal of the recovered **Ba[Co_2Fe_2-WS]** sample appears above 530 eV, whereas CoO_x species give rise O1s signals at 529.8 eV.

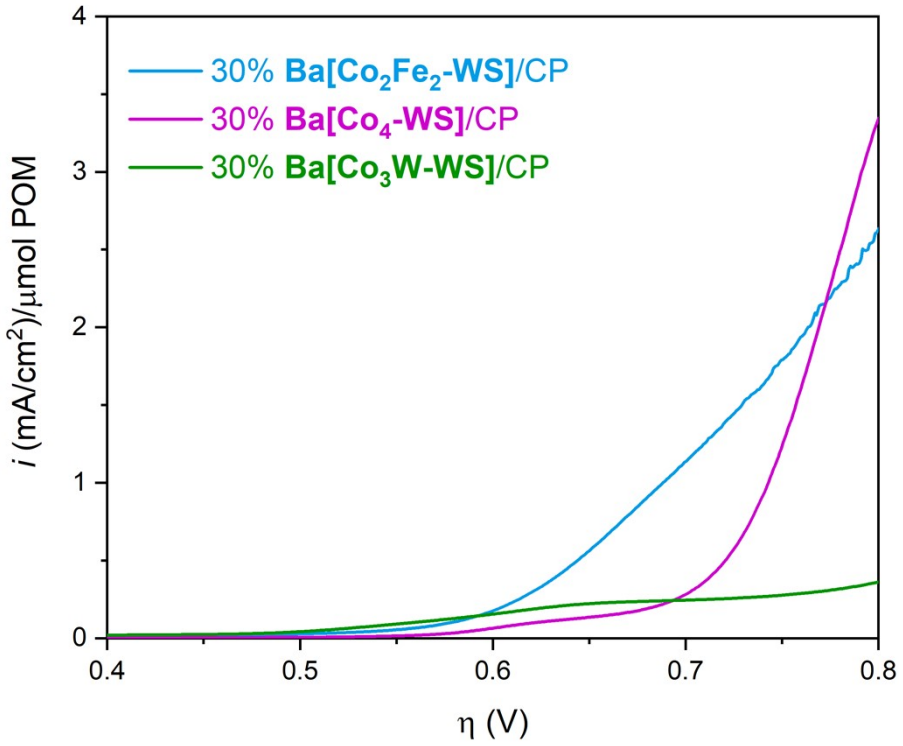

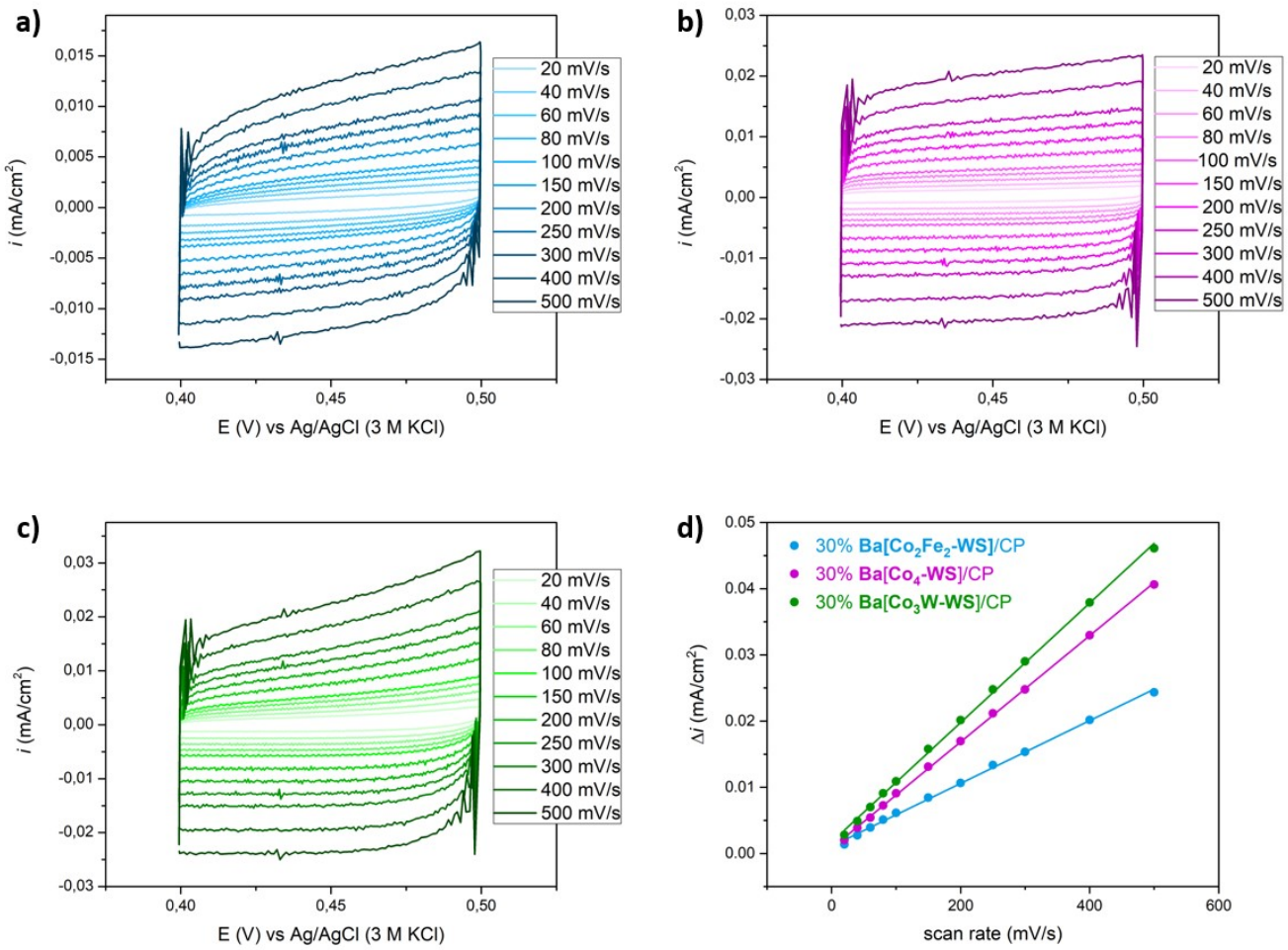

Fig. S18: Comparative LSV data of 30 wt.-% POM/CP electrodes normalized per µmol of POM used in each carbon blend (KP_i buffer at pH = 7.2).

Fig. S19: Comparison of the OER onset overpotential of 30 wt.-% POM/CP electrodes. The calculated values are 528 mV for **Ba[Co_2Fe_2-WS]** and 562 mV for **Ba[Co_4-WS]**.

Fig. S20: Double-layer capacitance (C_{dl}) measurements for 30 wt.-% POM/CP electrodes using a KP_i buffer at pH = 7.2. Cyclic voltammograms in the non-Faradaic region at different scan rates for **(a) Ba[Co_2Fe_2-WS]**, **(b) Ba[Co_4-WS]**, and **(c) Ba[Co_3W-WS]**; **(d)** Δi (i_a–i_c) *vs*. scan rate plot, where the slope = $2xC_{dl}$. The measured current does not arise from a Faradaic process and observed response arises from the charging of the double-layer. The calculated C_{dl} values are 23.72 µF/cm² for **Ba[Co_2Fe_2-WS]**, 40.12 µF/cm² for **Ba[Co_4-WS]**, and 45.14 µF/cm² for **Ba[Co_3W-WS]**.

Table S3: Elemental analysis (XPS) of freshly prepared samples of **Na[Co_2Fe_2-WS]**, **Ba[Co_2Fe_2-WS]**, and recovered **Ba[Co_2Fe_2-WS]** samples after bulk water electrolysis at 1 mA/cm^2. The ratios are normalised to the W content for direct comparison. The data is compared to expected theoretical values.

	Na	Ba	Co	Fe	W	O
Sample	Ratio (Atomic %)	Ratio (Atomic %)	Ratio (Atomic %)	Ratio (Atomic %)	Ratio (Atomic %)	Ratio (Atomic %)
Na[Co_2Fe_2-WS] theoretical	14 (12.96)	–	4 (3.70)	2 (1.85)	18 (16.67)	70 (64.81)
Na[Co_2Fe_2-WS] fresh	16.6 (15.51)	–	4.3 (4.05)	2.1 (2.00)	18.0 (47.48)	66.0 (6163)
Ba[Co_2Fe_2-WS] theoretical	0.6 (0.59)	6.7 (6.61)	4 (3.95)	2 (1.97)	18 (17.77)	70 (69.10)
Ba[Co_2Fe_2-WS] fresh*	0.3 (0.29)	9.6 (9.64)	1.2 (1.20)	1.5 (1.54)	18.0 (18.00)	69.4 (69.33)
Ba[Co_2Fe_2-WS] recovered*	0.0 (0.0)	10.2 (6.54)	3.1 (2.01)	2.6 (1.65)	18.0 (11.58)	121.6 (78.21)

***The deviation of metal content for the barium-containing samples before and after catalysis arises from the strong overlap of the Ba3d and Co2p XPS absorption bands, which precludes a detailed quantification of the elements.

Table S4: Elemental analysis (EDX) for freshly prepared **Na[Co_2Fe_2-WS]** and **Ba[Co_2Fe_2-WS]** samples and the recovered **Ba[Co_2Fe_2-WS]** sample after bulk water electrolysis at 1 mA/cm^2.The ratios are normalised to the W content for direct comparison. The data is compared to expected theoretical values.

	Na	Ba	Co	Fe	W
Sample	Ratio (Atomic %)	Ratio (Atomic %)	Ratio (Atomic %)	Ratio (Atomic %)	Ratio (Atomic %)
Na[Co_2Fe_2-WS] theoretical	14 (36.84)	–	4 (10.53)	2 (5.26)	18 (47.37)
Na[Co_2Fe_2-WS] fresh	13.8 (36.41)	–	4.1 (10.72)	2.0 (5.39)	18.0 (47.48)
Ba[Co_2Fe_2-WS] theoretical	0.6 (1.92)	6.7 (21.41)	4 (12.78)	2 (6.39)	18 (57.51)
Ba[Co_2Fe_2-WS] fresh	0.7 (2.16)	6.5 (20.76)	3.9 (12.54)	2.1 (6.79)	18.0 (57.75)
Ba[Co_2Fe_2-WS] recovered	0.0 (0.0)	6.6 (21.47)	3.9 (12.85)	2.1 (6.94)	18.0 (58.75)

8) Computational Details and Results

All calculations presented in this study were carried in Gaussian-16 package.[24] The B3LYP functional[25–27] was used together with the 6-31G(d,p) basis set for all hydrogens and oxygen bonded to the four central metal atoms while the 6-31G basis set was used for the rest of the oxygens.[28–30] The LANL2DZ effective core potential (ECP) and associated basis sets were used for the W, Co and Fe atoms.[31] All species were optimized in solution using the continuum model IEF-PCM with the Gaussian-16 defaults for water (ε = 78.36 and UFF radii).[32] The computational methodology was selected in basis of previous experience and with the aim of being able to compare results.[7,10] The nature of all the stationary points was verified by computation of the vibrational frequencies. All energies reported correspond to free Gibbs energies in solution in eV; computed potentials of electrochemical steps are reported in V and referred to NHE. A collection data set of all computational data is accessible in the ioChem-BD repository.[33]

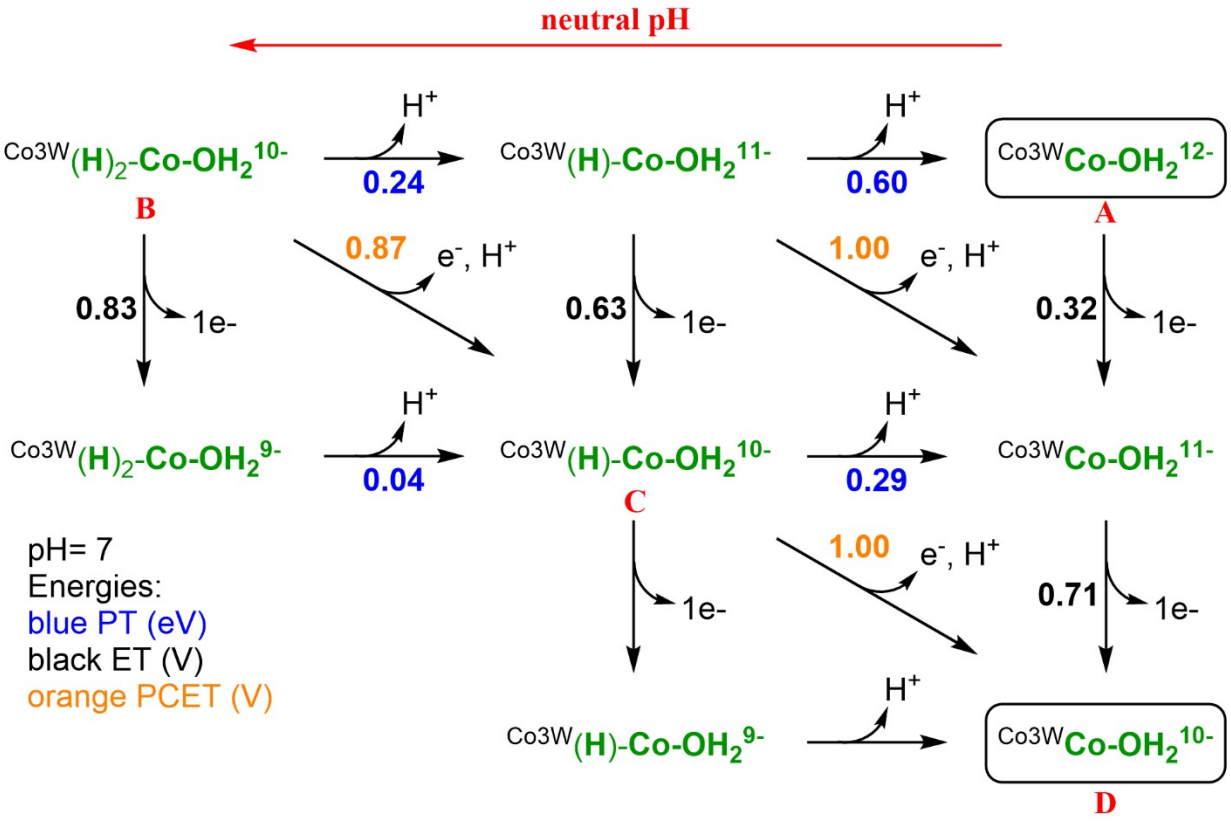

Fig. S21: Square diagram of the computed initial PCET, ET and PT events for the water oxidation reaction catalysed by the **Co_3W-WS** system. Potentials are given in V vs. NHE at pH = 7.

Co_3W-WS system

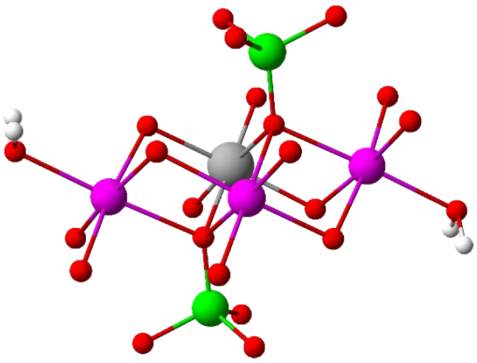

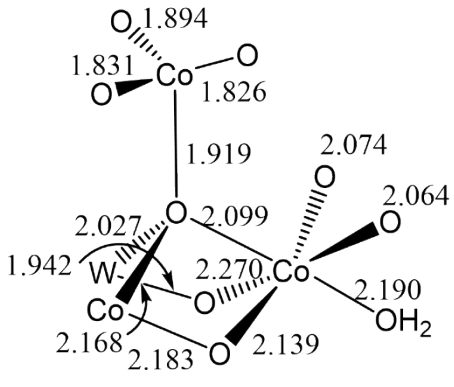

Co_2Fe_2-WS system

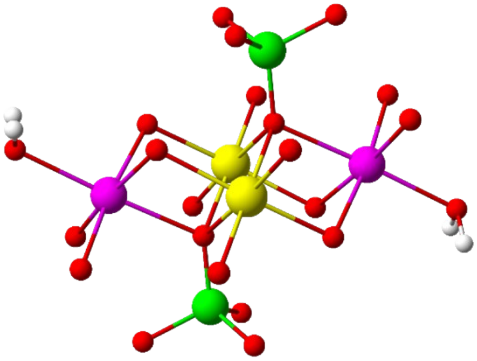

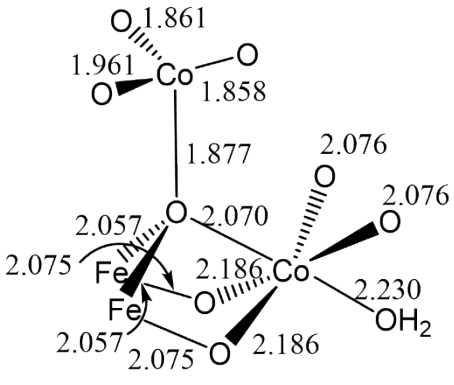

Co_4-WS system

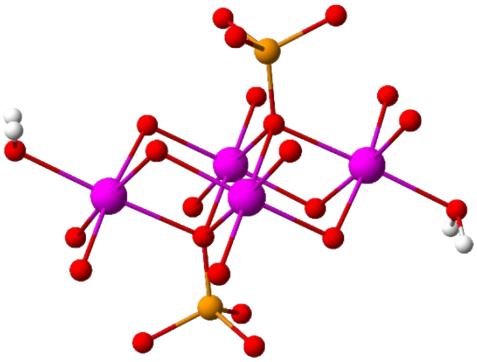

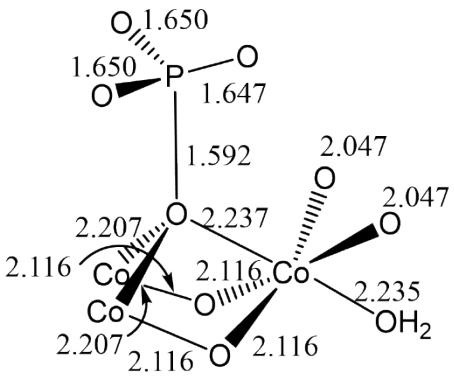

Extracted from J. Catal., 2017, 350, 56-63

Fig. S22: Schematic representation of key structural moiety of the **Co_3W-WS**, **Co_2Fe_2-WS** and **Co_4-WS** systems. Distances are given in Angstroms.

9) Supporting References

1 Bruker, SAINT+, Version 7.68, Bruker-AXS Inc, Madison, Wisconsin, USA, 2009.

2 Bruker, SADABS, Version 2004/1, Bruker-AXS Inc, Madison, Wisconsin, USA, 2004.

3 G. M. Sheldrick, *Acta Crystallogr. Sect. A Found. Adv.*, 2015, **71**, 3–8.

4 G. M. Sheldrick, *Acta Crystallogr. Sect. A Found. Crystallogr.*, 2008, **64**, 112–122.

5 O. V. Dolomanov, L. J. Bourhis, R. J. Gildea, J. A. K. Howard and H. Puschmann, *J. Appl. Crystallogr.*, 2009, **42**, 339–341.

6 F. Song, Y. Ding, B. Ma, C. Wang, Q. Wang, X. Du, S. Fu and J. Song, *Energy Environ. Sci.*, 2013, **6**, 1170–1184.

7 K. Azmani, M. Besora, J. Soriano-López, M. Landolsi, A.-L. Teillout, P. de Oliveira, I.-M. Mbomekallé, J. M. Poblet and J.-R. Galán-Mascarós, *Chem. Sci.*, 2021, **12**, 8755–8766.

8 P.-E. Car, M. Guttentag, K. K. Baldridge, R. Alberto and G. R. Patzke, *Green Chemistry*, 2012, **14**, 1680–1688.

9 H. Lv, J. Song, Y. V. Geletii, J. W. Vickers, J. M. Sumliner, D. G. Musaev, P. Kögerler, P. F. Zhuk, J. Bacsa, G. Zhu and C. L. Hill, *J. Am. Chem. Soc.*, 2014, **136**, 9268–9271.

10 J. Soriano-López, D. G. Musaev, C. L. Hill, J. R. Galán-Mascarós, J. J. Carbó and J. M. Poblet, *J. Catal.*, 2017, **350**, 56–63.

11 B. Liu, E. N. Glass, R.-P. Wang, Y.-T. Cui, Y. Harada, D.-J. Huang, S. Schuppler, C. L. Hill and F. M. F. de Groot, *Phys. Chem. Chem. Phys.*, 2018, **20**, 4554–4562.

12 M. Martin-Sabi, J. Soriano-López, R. S. Winter, J.-J. Chen, L. Vilà-Nadal, D.-L. Long, J. R. Galán-Mascarós and L. Cronin, *Nat. Catal.*, 2018, **1**, 208–213.

13 S. Goberna-Ferrón, J. Soriano-López and J. R. Galán-Mascarós, *Inorganics*, 2015, **3**, 332–340.

14 M. Tao, Q. Yin, A. L. Kaledin, N. Uhlikova, X. Lu, T. Cheng, Y.-S. Chen, T. Lian, Y. V. Geletii, D. G. Musaev, J. Bacsa and C. L. Hill, *Inorg. Chem.*, 2022, **61**, 6252–6262.

15 Z. Wang, X. Xin, Z. Li, M. Zhang, J. Zhang, Y. Feng, J. Zhang, H. Lv and G.-Y. Yang, *Sci. China Chem.*, 2023, **66**, 1771–1780.

16 A. Haider, B. S. Bassil, J. Soriano-López, H. M. Qasim, C. Sáenz de Pipaón, M. Ibrahim, D. Dutta, Y.-S. Koo, J. J. Carbó, J. M. Poblet, J. R. Galán-Mascarós and U. Kortz, *Inorg Chem*, 2019, **58**, 11308–11316.

17 M. Blasco-Ahicart, J. Soriano-López, J. J. Carbó, J. M. Poblet and J. R. Galán-Mascarós, *Nat. Chem.*, 2018, **10**, 24–30.

18 T. J. R. Weakley, H. T. Evans, J. S. Showell, G. F. Tourné and C. M. Tourné, *J. Chem. Soc., Chem. Commun.*, 1973, 139–140.

19 J. T. Arens, M. Blasco-Ahicart, K. Azmani, J. Soriano-López, A. García-Eguizábal, J. M. Poblet and J. R. Galán-Mascarós, *J. Catal.*, 2020, **389**, 345–351.

20 C. S. Ayingone Mezui, P. de Oliveira, A.-L. Teillout, J. Marrot, P. Berthet, M. Lebrini and I. M. Mbomekallé, *Inorg. Chem.*, 2017, **56**, 1999–2012.

21 H. Andres, J. M. Clemente-Juan, M. Aebersold, H. U. Güdel, E. Coronado, H. Büttner, G. Kearly, J. Melero and R. Burriel, *J. Am. Chem. Soc.*, 1999, **121**, 10028–10034.

22 H. Andres, M. Aebersold, H. U. Güdel, J. M. Clemente, E. Coronado, H. Büttner, G. Kearly and M. Zolliker, *Chem. Phys. Lett.*, 1998, **289**, 224–230.

23 J. M. Clemente-Juan, E. Coronado, A. Gaita-Ariño, C. Giménez-Saiz, H.-U. Güdel, A. Sieber, R. Bircher and H. Mutka, *Inorg. Chem.*, 2005, **44**, 3389–3395.

24 Gaussian 16, Revision C.01, M. J. Frisch, G. W. Trucks, H. B. Schlegel, G. E. Scuseria, M. A. Robb, J. R. Cheeseman, G. Scalmani, V. Barone, G. A. Petersson, H. Nakatsuji, X. Li, M. Caricato, A. V. Marenich, J. Bloino, B. G. Janesko, R. Gomperts, B. Mennucci, H. P. Hratchian, J. V. Ortiz, A. F. Izmaylov, J. L. Sonnenberg, D. Williams-Young, F. Ding, F. Lipparini, F. Egidi, J. Goings, B. Peng, A. Petrone, T. Henderson, D. Ranasinghe, V. G. Zakrzewski, J. Gao, N. Rega, G. Zheng, W. Liang, M. Hada, M. Ehara, K. Toyota, R. Fukuda, J. Hasegawa, M. Ishida, T. Nakajima, Y. Honda, O. Kitao, H. Nakai, T. Vreven, K. Throssell, J. A. Montgomery, Jr., J. E. Peralta, F. Ogliaro, M. J. Bearpark, J. J. Heyd, E. N. Brothers, K. N. Kudin, V. N. Staroverov, T. A. Keith, R. Kobayashi, J. Normand, K. Raghavachari, A. P. Rendell, J. C. Burant, S. S. Iyengar, J. Tomasi, M. Cossi, J. M. Millam, M. Klene, C. Adamo, R. Cammi, J. W. Ochterski, R. L. Martin, K. Morokuma, O. Farkas, J. B. Foresman, and D. J. Fox, Gaussian, Inc., Wallingford CT, 2016.

25 C. Lee, W. Yang and R. G. Parr, *Phys. Rev. B*, 1988, **37**, 785–789.

26 A. D. Becke, *J. Chem. Phys.*, 1992, **96**, 2155–2160.

27 P. J. Stephens, F. J. Devlin, C. F. Chabalowski and M. J. Frisch, *J. Phys. Chem.*, 1994, **98**, 11623–11627.

28 M. M. Francl, W. J. Pietro, W. J. Hehre, J. S. Binkley, M. S. Gordon, D. J. DeFrees and J. A. Pople, *J. Chem. Phys.*, 1982, **77**, 3654–3665.

29 W. J. Hehre, R. Ditchfield and J. A. Pople, *J. Chem. Phys.*, 1972, **56**, 2257–2261.

30 P. C. Hariharan and J. A. Pople, *Theor. Chim. Acta*, 1973, **28**, 213–222.

31 P. J. Hay and W. R. Wadt, *J. Chem. Phys.*, 1985, **82**, 270–283.

32 E. Cancès, B. Mennucci and J. Tomasi, *J. Chem. Phys.*, 1997, **107**, 3032–3041.

33 M. Álvarez-Moreno, C. de Graaf, N. López, F. Maseras, J. M. Poblet and C. Bo, *J. Chem. Inf. Model.*, 2015, **55**, 95–103.